International Journal of Solids and Structures 283 (2023) 112493

Contents lists available at ScienceDirect

International Journal of Solids and Structures

journal homepage: www.elsevier.com/locate/ijsolstr

Fracture analysis of multifunctional fiber-reinforced concrete using phase-field method

Amirreza Sadighi [a], Ebrahim Maghami [a], Mohammad Houshmand Khaneghahi [b], Divya Kamireddi [c], Seyed Ali Rahmaninezhad [b], Yaghoob (Amir) Farnam [b], Christopher M. Sales [b], Caroline L. Schauer [c], Ahmad R. Najafi [a,*]

[a] Department of Mechanical Engineering and Mechanics, Drexel University, Philadelphia, PA 19104, USA
[b] Department of Civil, Architectural, and Environmental Engineering, Drexel University, Philadelphia, PA 19104, USA
[c] Department of Materials Science and Engineering, Drexel University, Philadelphia, PA 19104, USA

ARTICLE INFO

Keywords:
Fiber-reinforced concrete
Finite element method
Crack propagation
Phase-field fracture
Fracture mechanics

ABSTRACT

In this paper, a numerical analysis has been conducted to predict the fracture response of a novel type of fiber-reinforced concrete blocks, called "multi-functional fiber reinforced concretes" (MFRCs). In MFRCs, fibers have been coated with a shell. This will allow the structure to be used for multiple purposes, including concrete self-healing. This study is conducted utilizing phase-field fracture framework. The shell thickness and the ratio of fiber length to diameter are the geometrical parameters whose effects on the fracture resistance of the MFRCs have been analyzed. As choosing the right shell material is under investigation, in the next step of the study, in addition to the geometrical factors, different material mismatch cases for the critical energy release rate of the shell has been analyzed. Moreover, the application of two different fibers, polyester fiber and polypropylene fiber (with almost 10 times higher critical energy release rate), are looked into. All the structures undergo three loading conditions: tensile loading, compressive loading, and three-point bending. In order to judge what configuration performs best, the values of peak force and absorbed energy of each structure in each case study have been taken into consideration and compared with those of other structures. It was seen that the most favorable performance and configuration depend on the loading condition and also the material set. Under tension, MFRCs with the lowest fiber length to diameter ratio exhibit the highest peak force and absorbed energy in the case of polyester fiber. The same observation was made for all models and material sets under compressive loading. Under three-point bending loading condition, for the cases of polyester fiber, similar results were obtained as the lowest fiber length to diameter ratio showed the best mechanical response. Having said that, it must be mentioned that shell material had a dominant effect on the fracture response of the structure under this loading condition. Polypropylene fibers also managed to increase the peak forces in different loading conditions.

1. Introduction

Concrete is the most commonly used construction material in the world owing to the fact that its characteristics can be modified in order to meet the needs of a wide variety of applications. However, concrete without reinforcement is brittle, a quality which is observed frequently in high-strength concrete (Mindess, 2008; Graham et al., 2013; Shah and Ribakov, 2011; Deng, 2005). Therefore, fiber-reinforced concretes (FRCs), with micro- and macro-fibers made of various materials, have been successfully utilized in construction and repair of structures and bridges (Banthia, 1994). This is due to the fact that they have considerable benefits in terms of resistance to fatigue and versality of use, as well as tangible higher strength. Moreover, such structures have attracted attention due to their high flexural strength, toughness and low drying shrinkage (Chen and Chung, 1996a; Fu and Chung, 1996; Chen et al., 1997). What is more, the fracture which happens due to plastic shrinkage cracking can be controlled better (Grzybowski and Shah, 1990; Kizilkanat et al., 2015) and a strain hardening characteristic can be added to the traditionally brittle structure (Li et al., 2001). It has been observed that crack growth in fiber-reinforced concretes is confined to values far lower than those without the reinforcement (Chen and Chung, 1996b). A number of investigations have been conducted to assess the fracture and fatigue response of FRCs (Swamy, 1979;

* Corresponding author.
E-mail address: arn55@drexel.edu (A.R. Najafi).

https://doi.org/10.1016/j.ijsolstr.2023.112493
Received 15 March 2023; Received in revised form 14 August 2023; Accepted 19 September 2023
Available online 29 September 2023

Shah, 1990; Zhang and Tang, 2021; You et al., 2017). In a study, it was displayed that the resistance of FRCs plunges owing to the multiple cycles of fiber pull-out and push-in during the early stages (Fu and Chung, 1996). Moreover, the boost in the toughness of FRCs by implementing fibers of 6–10 mm was proven experimentally by Banthia et al. (1994) and Banthia and Sheng (1996). It was concluded that with a volume fraction of 1%, 2%, 3% of carbon fiber, both load-carrying capacity and toughness rises considerably. In another study, the tensile and flexural properties of cementitious composites reinforced with very short fibers were looked into (length of fibers was $1\frac{1}{4}$ mm) (Mobasher and Li, 1996). It was realized that when the length of the fibers is below a certain value, the results are not favorable.

Deng investigated the fracture and fatigue response of carbon FRCs under flexural loading (Deng, 2005). He proved the critical effective crack length for carbon fiber reinforced concrete (CFRCs) is considerably increased in comparison with that of plain concrete, regardless of the pre-cyclic loading history and fatigue life. Also, the beneficial effects of implementing carbon-fiber laminates in the concrete beams on their shear strength were analyzed by Zhang and Hsu (2005), exhibiting that the CFRP can tangibly increase the ductility and ultimate shear strength of concrete. Furthermore, it added the benefit of better serviceability to the structure. Turgay et al. (2010) conducted experiments on square fiber-reinforced concrete columns in a larger scale, revealing that with a rise in the diameter of transverse reinforcement, a higher ductility can be achieved while the ultimate strength of columns almost stays unchanged.

Failure mechanisms of FRCs is well explained in a number of previous research, probably best by the Aveston, Cooper, and Kelly (ACK) model of multiple cracking (Aveston and Kelly, 1973). However, it is worth pointing out that these beneficial effects of fiber-reinforcement concretes greatly depend on how strong the bonding is between the fibers and cementous paste. In other words, the friction during the pull-out or debonding of the fiber increases the work required to fracture the FRCs, thereby raising its fracture toughness. If wisely tuned, this phenomenon also encourages stable crack growth and multiple cracking in the matrix (Li et al., 2002; Lee and Jacobsen, 2011; Yoo et al., 2015a, 2013; Qian and Stroeven, 2000; Stroeven and Babut, 1986). For instance, in another study, Stynoski et al. (2015) also revealed that it is necessary to optimize the dosage, size, and interface strength to fully implement carbon fibers and nanotubes in concrete. Another point that dominates the amount of improvement is the fiber volume fraction (Bažant and Planas, 2019; Kizilkanat, 2016). The different types of fiber, including asbestos, cellulose, steel, polypropylene, PVA, carbon, basalt, aramid, polyethylene and glass, also determine how much strength can be added to the structure (Owens et al., 2003). For instance, in one study, Kizilkanat et al. (2015) proved that, although under debate by some, there was no significant effect of basalt fiber inclusion on the compressive strength and elastic modulus of concrete. However, the fracture energy increased significantly after 0.25% dosage for both basalt and glass reinforced concrete. In the same study it was also found that adding polymers to ordinary concrete can improve the bonding between the aggregate and the cement stone and also its deformation performance. Moreover, it can increase the dispersion of fiber in concrete and strengthen the bonding interface between fiber and matrix. The bonding can also effectively improve the fracture response of the structure (Alam and Loukili, 2020; Bažant and Oh, 1983; Sun and Xu, 2008; Bărbuţă et al., 2010; Cao et al., 2012). In an investigation, it was also shown that both carbon fiber or polymer latex powder can increase the split tensile strength and peak strain of concrete (Meng et al., 2021).

Another important aspect that nowadays has drawn a lot of attention to itself is the service life of concrete structures, which can be extended by using self-healing concrete and lower their maintenance cost (De Belie et al., 2018). Diverse self-healing concretes have been developed, including using different methods, such as crystalline admixture (Ferrara et al., 2016), minerals (Qureshi et al., 2019), polymers (Mignon et al., 2015; Snoeck et al., 2018), bacteria (Gupta et al., 2017), microencapsulation (Milla et al., 2019), and encapsulations (Al-Tabbaa et al., 2019). Among these smart self-healing techniques, encapsulation-based self-healing composites have unique advantages, in terms of service life and the capacity to recover the mechanical strength. Furthermore, it has been shown that the encapsulation based self-healing technique can assist the concrete structure to seal cracks larger than 900 μm (Xue et al., 2019). In the encapsulation-based self-healing system, healing agent is stored in a carrier, which is first broken, and subsequently released into crack space (Giannaros et al., 2016). The healing agent can adhere to two crack surfaces when it turns into solid, and thus seal the crack. At the same time, the bonding interfaces are generated between healing agent and crack surfaces. It would be ideal if this interface is able to tolerate the loading without separation during reloading. However, some relevant research has demonstrated that the self-healing performance of encapsulation-based self-healing concretes is not always favorable because of the debonding between the healing agent and the crack surface (Gilabert et al., 2017). This bonding behavior also relies on the amount of healing agent and mechanical properties of the crack surface (Xue et al., 2020).

In order to have further investigations into the fracture response of concrete under different types of loading, different methods have been utilized to numerically simulate the fracture. Finite element method (FEM) has provided a fundamental technique to deal with the discontinuity problems such as cracks (Schlangen, 1995). However, the standard FE formulation limited capability to follow crack propagation, as it requires remeshing (Roth et al., 2015; Cervera et al., 2022; Rots et al., 1985; Jirásek and Zimmermann, 1998). Various computational methods have been developed to study mechanical fractures. The most commonly used methods are cohesive zone methods and the generalized/extended finite element methods (G/XFEMs) (Babuška et al., 2003; Gordeliy and Peirce, 2013, 2015; Park and Paulino, 2011; Belytschko and Gracie, 2007). The cohesive zone method (Matvienko, 1999; Elices et al., 2002; Lyu et al., 2016; Urata and Li, 2017) can analyze the fracture response of uncracked structures, including those with blunt notches, and is not limited to the response of bodies with pre-cracks. However, the accuracy of cohesive zone methods, similar to standard finite element method, greatly depends on the quality of mesh, hence, mesh refinement is a necessary step to eschew the convergence issues. This drawback does not apply to the G/XFEM (Turgay et al., 2010), which gained a lot of popularity due to its capability to model complicated geometries that are independent of mesh and no remeshing is needed as crack grows (Babuška and Banerjee, 2012; Strouboulis et al., 2000; Sukumar et al., 2000; Roth et al., 2015; Karihaloo and Xiao, 2003; Colombo, 2012; Areias and Belytschko, 2005; Duarte et al., 2001; Gordeliy et al., 2019). Nonetheless, this technique might face a challenge to adapt to complex cracks morphologies (especially for the cases where crack branching and merging occurs in 3D FEA) because of the underlying level-set functions needed to describe the displacement jump (Nguyen et al., 2016b; Jirásek and Belytschko, 2002).

Over the recent decade, however, attentions have been drawn to the simulation of fracture using phase field method as it solves three major limitations of linear elastic fracture mechanics: (1) forbidden crack initiation, (2) the existence of stress singularity at the crack tip and (3) the necessity to have an external fracture criteria (Nguyen et al., 2016a). Phase field modeling has been utilized in various investigations in fracture mechanics (Li and Xu, 2022; Wu and Chen, 2022; Nguyen et al., 2020; Aldakheel et al., 2018; Nguyen et al., 2016b; Khisamitov and Meschke, 2018; Tanné et al., 2018; Zhou et al., 2018; Molnár and Gravouil, 2017). This method has been implemented in a wide range of fields, including fracture in concrete (Schröder et al., 2022; Feng and Wu, 2018; Yang et al., 2019), composite (Xia et al., 2018; Bui and Hu, 2021), bone and dentin (Maghami et al., 2021b,a; Maghami and Najafi, 2022; Maghami et al., 2022; Josephson et al., 2022). A combination of energy-based phase field model was used for fracture with classical zero-thickness interface models for crack analysis with

a staggered approach (Khisamitov and Meschke, 2018). In this diffuse crack analysis approach, not only is the prescription of the crack not required, but also complex crack tracking is possible (Natarajan et al., 2019). Furthermore, this method can simulate crack merging and crack branching in complex morphologies with a straightforward implementation (Ambati et al., 2015). After reviewing the state-of-the-art, we realized that while the cohesive zone models (Park et al., 2010; Rabczuk et al., 2008; Unger et al., 2007; Elices et al., 2009) and G/XFEM models (Roth et al., 2015; Kozlowski et al., 2016; Ren and Li, 2013; Asferg et al., 2007) have been utilized to look into the fracture behavior of concretes, very few studies have been conducted to exploit the PFM and have a parametric study on the fracture response of fiber-reinforced concretes.

In the present study, we look into the crack initiation and propagation in multifunctional fiber reinforced concrete blocks (MFRCs). These multifunctional fibers are intended to increase the flexural strength of the concrete blocks. Moreover, they encompass a shell, adding the factor of multifunctionality. With a desirable mechanical property, the shell can be exploited so that as the crack propagates through the matrix and approaches the fibers, it is deflected and propagates through the interface (shell). In addition to crack propagating through the interface, crack bridging could be achieved with favorable mechanical property of the shell. With crack bridging phenomenon, instead of the main crack propagating through the fibers, there will be multiple smaller cracks in the concrete that are easier to be healed. Additionally, the energy absorption capacity of the structure increases. Furthermore, the shells can carry microbial-based healing agent for self-healing purposes. However, the focus of the present study is on strengthening the bonding and managing the crack propagation by exploiting the shell. Therefore, using PFM, we investigate the fracture response of MFRCs under three different types of loading: tension, compression, and three-point bending. To the best of our knowledge, there have been very few comprehensive studies which simultaneously take into consideration the effect of geometrical parameters and material property mismatch of the fiber and shell on the mechanical response and fracture resistance of MFRCs. Accordingly, in the present study, we consider varied values of fiber length, fiber diameter and shell thickness based on the experiments going on in our labs and analyze how the fracture resistance of the concrete blocks change with different geometrical characteristics of fiber and shell. In the next stage, the effect of using different material sets will be studied to investigate the fracture response of the blocks. Finally, the energy absorption and the peak force of each of the structures are compared with those of one another to conclude what geometrical characteristic and material set show the most favorable performance under each loading type.

2. Materials and methods

2.1. Phase-field problem statement

We begin with an arbitrary n-dimensional domain $\Omega \in R^n$, which is used to represent a solid body including an internal crack $\Gamma \subset R^{n-1}$, and with external boundaries of the body $\partial\Omega \subset R^{n-1}$ (Fig. 1). The aim is to look into the crack propagation in the body within the time range of $\tau \subset R$. Diffusive fracture, which was originally developed in Miehe et al. (2010), has been adopted in this study, through which a coupled two-field problem is defined to represent the phase-field damage model. The first field is displacement, as below

$$\boldsymbol{u} = \begin{cases} \Omega \times \tau \rightarrow R^n \\ (\boldsymbol{x}, t) \rightarrow \boldsymbol{u}(\boldsymbol{x}, t) \end{cases} \tag{1}$$

where $\boldsymbol{u}(\boldsymbol{x}, t)$ is the displacement vector of material point x at time $t \in \tau$. The second field is the crack phase field, defined as below on the body Ω

$$d = \begin{cases} \Omega \times \tau \rightarrow [0, 1] \\ (\boldsymbol{x}, t) \rightarrow d(\boldsymbol{x}, t) \end{cases} \tag{2}$$

where d is an auxiliary field, with $d(\boldsymbol{x}, t) = 1$ denoting the fully damaged state and $d(\boldsymbol{x}, t) = 0$ representing the intact area. Moreover, the diffusive crack, defined by the regularized crack function of damage variable d, can be differentiated from a sharp crack topology as shown in Fig. 1.

Total potential of the crack body is taken in the following form in order to couple the displacement and phase-field damage problem

$$\Pi^{tot} = E(\boldsymbol{u}, d) + W^{dmg}(d), \tag{3}$$

where $E(\boldsymbol{u}, d)$ is the elastic energy restored in the cracked body and $W^{dmg}(d)$ is the work needed to create the cracks in the body. The former term can be computed as

$$E(\boldsymbol{u}, d) = \int_{\Omega} \Psi(\boldsymbol{\varepsilon}(\boldsymbol{u}), d)\, d\Omega, \tag{4}$$

where $\Psi(\boldsymbol{\varepsilon}(\boldsymbol{u}), d)$ is the strain energy density for the cracked body and $\boldsymbol{\varepsilon}(\boldsymbol{u})$ is the symmetric strain tensor. In order to study the relationship between the stress tensor and degraded strain energy, readers are referred to Miehe et al. (2010). The latter term in Eq. (3), is the work to create the crack in the body, which can be written as

$$W^{dmg}(d) = \int_{\Omega} G_c\, \gamma(d, \nabla d)\, d\Omega, \tag{5}$$

where G_c is the critical energy release rate and $\gamma(d, \nabla d)$ is the crack density function first explained in (Bourdin et al., 2008)

$$\gamma(d, \nabla d) = \frac{1}{2l_c} d^2 + \frac{l_c}{2} \nabla d \,.\, \nabla d, \tag{6}$$

where l_c is the length scale parameter, characterizing the width of the regularization zone between the broken and unbroken states of material.

In order to compute the two fields, the problem can be separated into two independent minimization formulations. Fig. 2 exhibits how these two separated fields can be linked to each other using a history field. In the first problem, the energy functional arising from the phase field takes the following form in order to solve the fracture topology

$$\Pi^{d} = \int_{\Omega} \left(G_c \gamma(d, \nabla d) + (1 - d^2)\, \mathcal{H} \right) d\Omega, \tag{7}$$

where $\mathcal{H}$ is the history functional to assure the irreversibility of the damage in the body. This term has been more in-detail explained in Miehe et al. (2010). In the second problem, following upon the first problem, by considering the attained d to be constant, the energy functional for the displacement takes the form as below

$$\Pi^{u} \simeq E(\boldsymbol{u}, d) - W^{ext}, \tag{8}$$

where W^{ext} is the external work arising from the body forces and tractions imposed upon the body as below

$$W^{ext} = \int_{\Omega} \bar{\boldsymbol{b}}.\boldsymbol{u}\, d\Omega + \int_{\partial\Omega} \bar{\boldsymbol{t}}.\boldsymbol{u}\, d\partial\Omega, \tag{9}$$

where $\bar{\boldsymbol{b}}$ and $\bar{\boldsymbol{t}}$ are body forces and the boundary tractions, respectively. By substituting Eqs. (4) and (9) into Eq. (8), displacement energy functional takes the form

$$\Pi^{u} = \int_{\Omega} (\Psi(\boldsymbol{\varepsilon}(\boldsymbol{u}), d) - \bar{\boldsymbol{b}}.\boldsymbol{u})\, d\Omega - \int_{\partial\Omega} \bar{\boldsymbol{t}}.\boldsymbol{u}\, d\partial\Omega. \tag{10}$$

By taking into consideration Eqs. (7) and (10), the strong forms of the phase field and displacement field can be obtained by calculating the variations of these two energy functionals. This scheme, as well as the framework, has been further expanded in Appendix A. Additionally, in case of the reader's interest, further information on this, as well as the FE discretization of this method, can be found in Miehe et al. (2010) and Nguyen et al. (2016b).

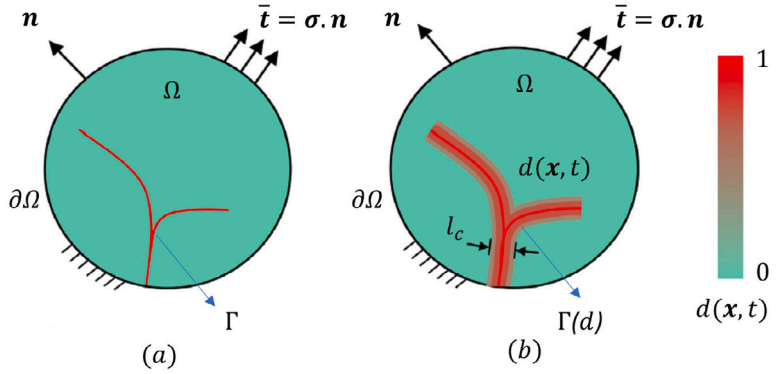

Fig. 1. Regularized representation of a crack through phase field (a) sharp crack, (b) diffusive crack.

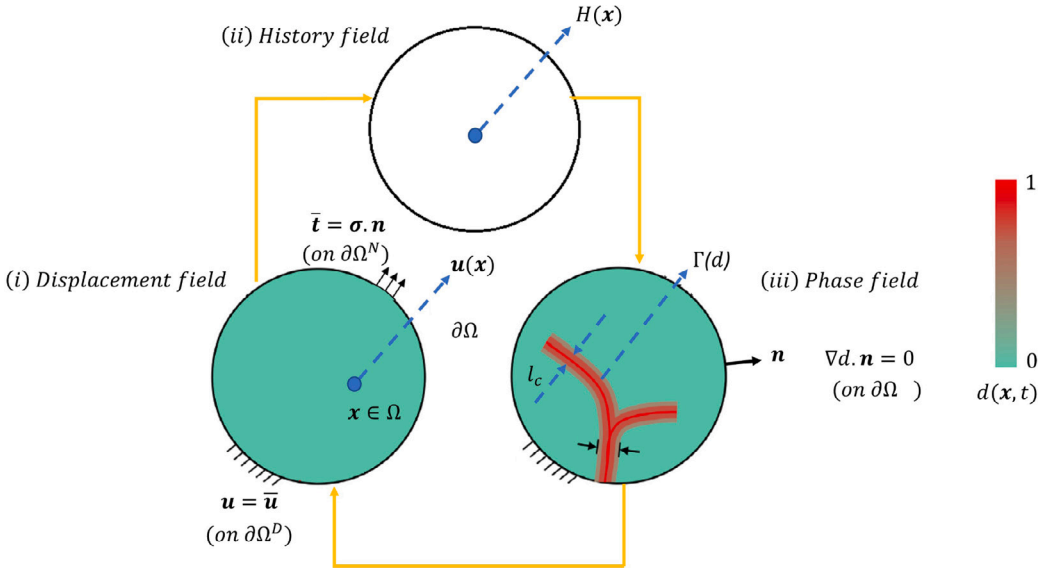

Fig. 2. A schematic representation of the relationship between the two fields through history field (The solid black arrows are vectors, and the dashed blue arrows represent different variables).

2.2. Finite element modeling and material properties

In order to solve the two-field problem in this paper, a user-defined element subroutine (UEL), developed by Molnár and Gravouil (2017), has been implemented in Abaqus (2021). We aim to investigate fracture evolution in MFRCs under different loading conditions. In this study, four-node elements and hexagonal elements have been utilized for the 2D and 3D models, respectively. Mesh convergence has been conducted and explained in detail in Appendix B. The smallest mesh size in the potential damage area (in front of the pre-cracks and around fibers and shells in the tension and three-point bending models) has been considered 0.05 mm. The same mesh size has been considered for the entire area of the compression models as there is no certain position for the initiation of cracks and microcracks. For all tension and compression models, as it can be seen in Fig. 3e and f, the bottom surface is fixed along y direction. For three-point bending, the bottom edges are fixed in y-direction (Fig. 3a). Moreover, in all of the models, the right edge of the models has also been fixed in x-direction. The 2D models have been imposed different displacement loading conditions of tension, compression, and three-point bending along y-direction. In 3D simulations, these blocks undergo a tensile displacement loading in y-direction, in the magnitude of 0.012 mm (Fig. 3). These loads have been applied to MFRCs in two different steps. To ensure the numerical stability and accuracy of the results, in the first step, the displacement load was applied up to the crack nucleation point (with increment sizes of 2.5×10^{-5} mm for the first 300 increments). From there, for the remainder of the displacement load, much smaller increments were employed (2.5×10^{-6} mm for the remaining increments) (Miehe et al., 2010; Molnár and Gravouil, 2017). In all models, the same length scale parameter of $l_c = 0.1$ mm has been used to define the crack width. Further explanation on length scale parameter can be found in Appendix B. The randomization process of the distribution and angle of fibers has been performed through a script using 'rand' function in MATLAB software (MATLAB, 2021). The dimensions of the tension and compression models are set to be 100×100 mm^2, while for the three-point bending study the dimensions are set to be 250×50 mm^2. For the 3D analysis, the dimensions of the MFRCs are $16 \times 16 \times 16$ mm^3.

There are three case studies considered in this paper.

- The first 2D case study is regarding the geometrical parameters. The effects of changing three geometrical parameters are considered on the fracture response of MFRCs. These parameters are: the fiber length (l), the fiber diameter (d), and the shell thickness (t). However, in order to reduce the number of models, the chosen parameters are the ratio of the fiber length to fiber diameter (l/d) and the shell thickness (t). There are two fibers considered here (polyester and polypropylene) with average diameters of 0.3 mm. For the ratio of the fiber length to fiber diameter (l/d), the magnitudes of 40, 50, and 60 have been considered, given that there are three conventional lengths considered for the fibers:

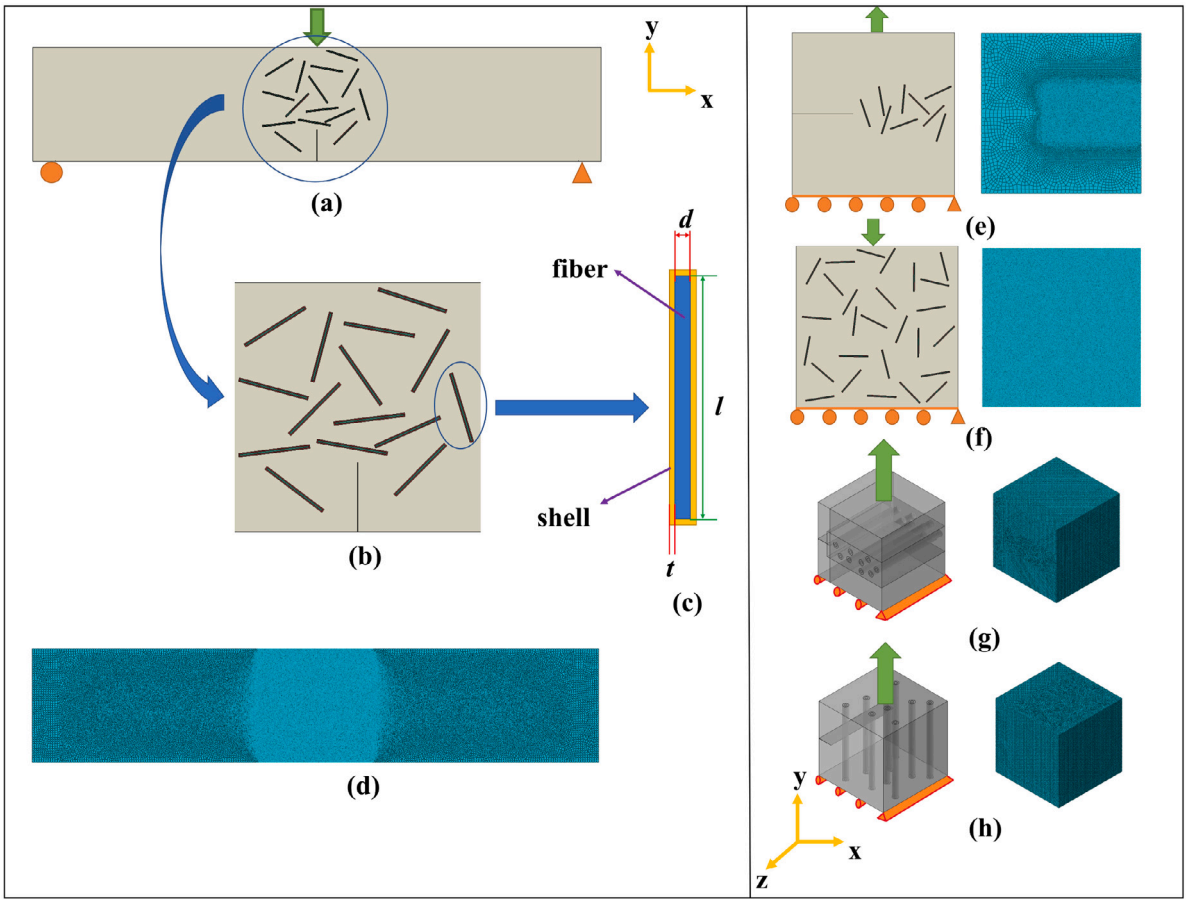

Fig. 3. Representation of the models (a) model under three-point bending, (b) closer look at the fibers and shells, (c) geometrical parameters of fibers and shells, (d) meshed model under three-point bending, (e) model under tension (f) model under compression, (g) 3D model with anti-parallel fibers under tension, (h) 3D model with perpendicular fibers under tension. Please note that distributed tensile and compressive loadings have been applied in the simulations.

Table 1
Geometrical parameters of MFRCs.

Model No.	l/d ratio	Shell thickness (t)
Model 1 (l/d = 40, t = 0.2)	40	0.2
Model 2 (l/d = 40, t = 0.3)	40	0.3
Model 3 (l/d = 40, t = 0.4)	40	0.4
Model 4 (l/d = 50, t = 0.2)	50	0.2
Model 5 (l/d = 50, t = 0.3)	50	0.3
Model 6 (l/d = 50, t = 0.4)	50	0.4
Model 7 (l/d = 60, t = 0.2)	60	0.2
Model 8 (l/d = 60, t = 0.3)	60	0.3
Model 9 (l/d = 60, t = 0.4)	60	0.4

12, 15, 18 mm. All of the models have a typical fiber volume fraction of 1–2% given the different fiber length to diameter ratios (Aydın and Baradan, 2013; Han et al., 2019). Based on the manufacturing process currently going on in our lab, in order to create the shell on the fibers, these fibers are coated with nitrocellulose, whose thickness is not reported to be uniform, but can range from 0.2 mm to 0.4 mm. Consequently, three different magnitudes have been chosen for the shell thickness. There are 3 cases considered for each of these two parameters, making the study of a total of 9 cases. For a more straight-forward approach to refer to the blocks, the geometrical parameters and numbering of the models have been tabulated in Table 1. As it can be seen, models 1–3, 4–6, and 7–9 have the l/d ratio of 40, 50, and 60, respectively. In each of the three sets, from the first model to the third one, the shell thicknesses are 0.2, 0.3, and 0.4, respectively. In this case study, these 9 models undergo the three loading conditions: tension, compression, and three-point bending (Fig. 3a, e, and f, respectively). At this step, considering the energy release rate (G), even though there is no information on the critical energy release rate of the shell material, as it is typically tougher than concrete, it is assumed that the material mismatch is $G_{Matrix} < G_{Shell} < G_{Core}$. This way, we will be able to focus on the geometrical parameters.

- In the second 2D case study, we look into the effects of material property mismatch and the variations in the energy release rate (G_c) of the fiber and shell on the final fracture response of the blocks under the same boundary conditions and three loading types shown in Fig. 3. Therefore, as the critical energy release rate of the concrete (matrix) and fibers (core) are known and fixed (Cao et al., 2019; Mansour et al., 2017; Bei-Xing et al., 2004), only the cases in Table 2 will be studied. In doing so, the different scenarios for different shell properties are taken into consideration. In all these material sets, the critical energy release rate of the fiber is deemed the highest. Material set 1, which is the material set considered in the first 2D case study explained above, consists of polyester fibers and presumes the shell material is tougher than concrete (tough shell). In material set 2 (average tough shell), the critical energy release rate of the shell and concrete are considered almost the same. In material set 3, critical energy release rate of the shell is assumed to be lower than of the concrete (less tough shell). Finally, in the material set 4, the effect of using a much tougher fiber, which in this paper is polypropylene fiber, is taken into consideration (almost 10 times tougher than polyester fiber). In this case, the material properties of shell and concrete are the same as those of material

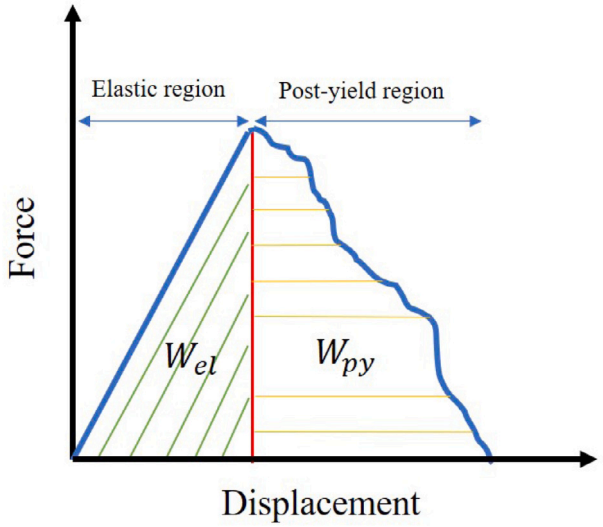

Fig. 4. The elastic energy absorbed W_{el} (left shaded area) and post-yield energy absorbed W_{py} (right shaded area). The end of the elastic region is the point where the first drop in the force–displacement result is observed. It is also considered the damage initiation point.

Table 2
Material mismatch cases.

Material set (1) $G_{Matrix} < G_{Shell} < G_{Core}$ (Polyester Fiber)	Material set (3) $G_{Shell} < G_{Matrix} < G_{Core}$ (Polyester Fiber)
Material set (2) $G_{Matrix} \simeq G_{Shell} < G_{Core}$ (Polyester Fiber)	Material set (4) $G_{Matrix} < G_{Shell} \ll G_{Core}$ (Polypropylene Fiber)

set 1. Moreover, as it can be checked in Table 3, the fracture energy of the polypropylene fiber is almost 10 times more than of the polyester fiber. This will require a total of 36 cases to be analyzed and compared, out of which 9 cases are from the first case study. The material properties of the fiber and concrete can also be checked in detail in Table 3.

- In the third case study, we perform a 3D FE analysis to look into the effects of fiber distribution on the mechanical response of the microstructure of MFRCs. In these 3D models, fibers have been placed anti-parallel and perpendicular with respect to the pre-crack (Fig. 3g and h). The aim is to compare the results and determine how the performance is affected when the majority of the fibers are perpendicular or parallel to the pre-crack and in which situation MFRCs exhibits a better mechanical response. Moreover, the effect of material property mismatch and the variations in the energy release rate (G_c) of the fiber on the final fracture response of the blocks are analyzed. In the 3D models of MFRCs, the fiber length and shell thickness are 12 and 0.3 mm, respectively.

3. Results

To assess the damage evolution in MFRCs, their force–displacement results have been considered to determine the peak force these structures can undergo (PF), as well as to calculate the absorbed energy (W_{tot}), which is the area under the force–displacement results (Fig. 4). This area is also representative of the toughness of the models. Furthermore, in order to have a more in-depth analysis on the crack growth resistance of MFRCs, in addition to the total absorbed energy (W_{tot}), post-yield energy absorption (W_{py}) of these structures have also been specified in the results section. To make it convenient for comparing the results, the above-mentioned criteria have been normalized according to the maximum value in each set of data. Moreover, for each set, these maximum values have been reported for the readers to be able to calculate the precise magnitudes of PF, W_{tot}, and W_{py}, as well as to compare the results between different material mismatch cases.

3.1. Fracture response of MFRCs under tension

In order to have a complete analysis on the response of the MFRCs under tensile loading, the force–displacement results are discussed along with the crack propagation through the blocks.

The crack propagation in the MFRCs can be observed in Fig. 5. The force–displacement (FD) results can be seen in Fig. 6. The first drop in the FD diagram stems from the crack initiation while the final drop is due to the failure of the structure.

The models with lower l/d values exhibit a higher peak force at the early stages of crack propagation and can withstand higher displacement loads before failure. Moreover, based on Fig. 6b and c, the general trend shows that with an increase in the shell thickness, the amount of energy absorption of the structure increases as the structure at a slightly higher displacement load fails (approaching 0.045 mm displacement load as the shell thickness increases). In order to have a more thorough investigation, Table 4 presents the normalized values of peak force and absorbed energy of MFRCs. For reference, the values of PF, W_{tot}, and W_{py} for model 1 are 16.37 J, 11.87 J, and 580.24 kN.

Table 4 shows that the highest amount of energy absorption and peak force is for the model 1, with $l/d = 40$ and $t = 0.2$ mm. However, concluding in general, it can be seen that for all other models, the rise in the shell thickness from 0.2 to 0.3 mm increases the peak force that MFRCs can undergo before it fails.

Table 3
Material properties of the fibers and concrete.

Material	Elastic modulus (MPa)	Poisson ratio	Energy release rate (N/m)
Concrete (Cao et al., 2019)	26510	0.19	503.027
Polyester (Mansour et al., 2017)	709.17	0.2	975.3
Polypropylene (Bei-Xing et al., 2004)	9109.4	0.2	10200

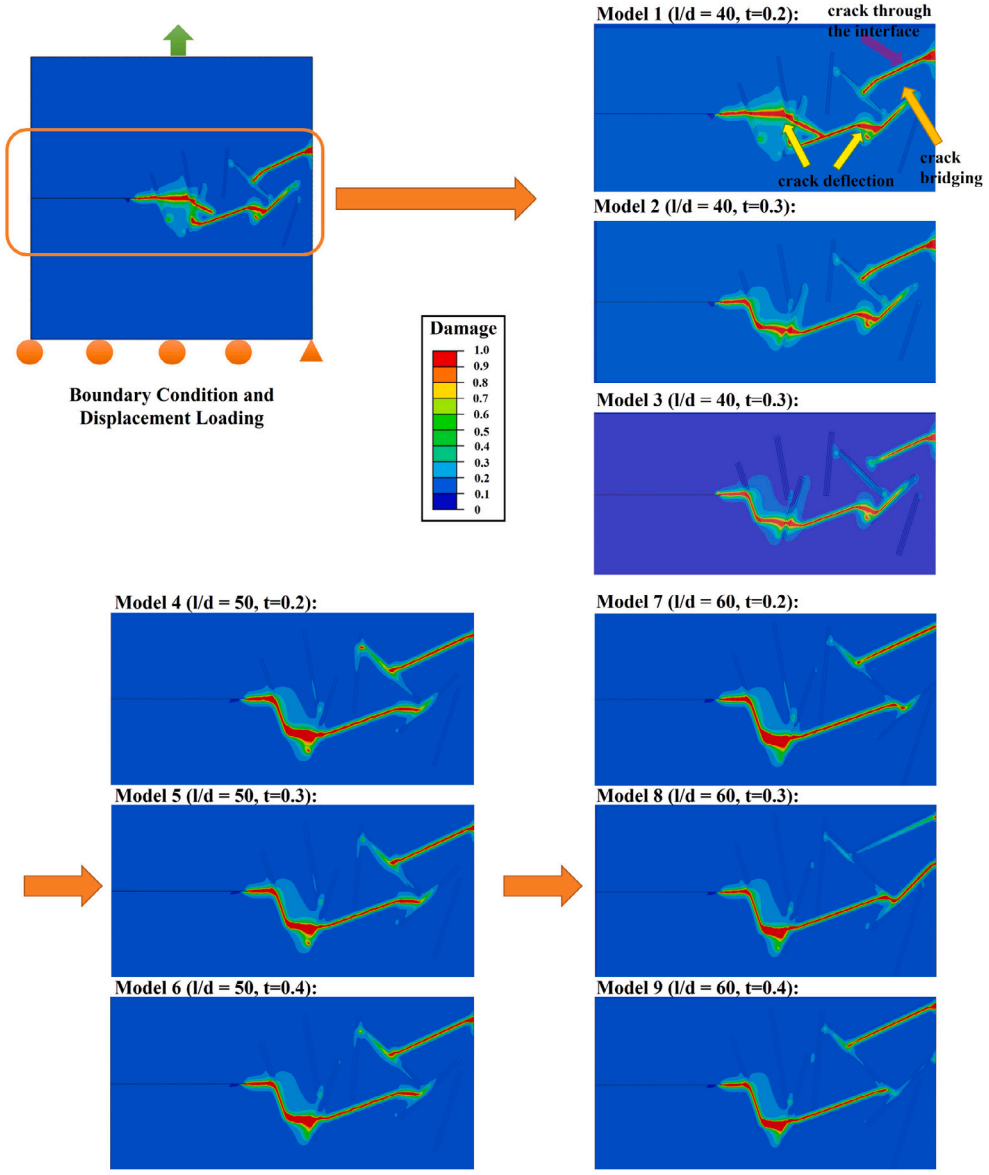

Fig. 5. The crack propagation in the MFRCs under tension. Crack propagates through the shell and concrete and is deflected due to higher critical energy release rate of fiber (shown in model 1). Crack bridging can also be seen, which increases the absorbed energy.

Table 4
Normalized values of energy absorption and peak force of MFRCs under tension. With this material set, model 1 shows the most favorable fracture response. For reference, the values of W_{tot}, W_{py}, and PF for model 1 are 16.37 J, 11.87 J, and 580.24 kN.

Model No.	W_{tot} (J)	W_{py} (J)	PF (kN)
Model 1	1	1	1
Model 2	0.970678	0.964617	0.985937
Model 3	0.971289	0.971356	0.976148
Model 4	0.854001	0.812131	0.844857
Model 5	0.917532	0.905644	0.884737
Model 6	0.910812	0.902275	0.865556
Model 7	0.859499	0.83235	0.84727
Model 8	0.924863	0.928391	0.902351
Model 9	0.932804	0.946083	0.875241

3.2. Fracture response of MFRCs under compression

The force–displacement results of the MFRCs under compression can be checked in Fig. 7. Table 5 also exhibits the normalized amount of absorbed energy as well as the peak force that these blocks exhibited under compression. It can be observed that lower l/d ratios and shell thickness result in higher energy absorption and peak force. More specifically, Model 1 has the highest W_{tot} (939.67 J), W_{py} (773.79), and PF (5639.20 kN), while model 9 has the lowest values. For a better understanding of the results mentioned above, the crack propagation is exhibited in Fig. 8.

3.3. Fracture response of MFRCs under three-point bending

For a better representation of crack propagation under three-point bending, as displayed in Fig. 9, only the central part of the blocks is shown.

Force–displacement results and normalized magnitudes of absorbed energy and peak force can be observed in Fig. 10 and Table 6, respectively. Similar to the results of the models under compression and tension, MFRCs have a better performance under three-point bending tests with lower l/d values. To illustrate, the highest magnitudes of W_{tot} and W_{py} are for model 3 (8.42 and 6.90 J, in the same order), while model 2 shows a slightly higher PF (69.60 kN). However, when the results are deemed in general (for instance, W_{tot} and W_{py} of model 6,

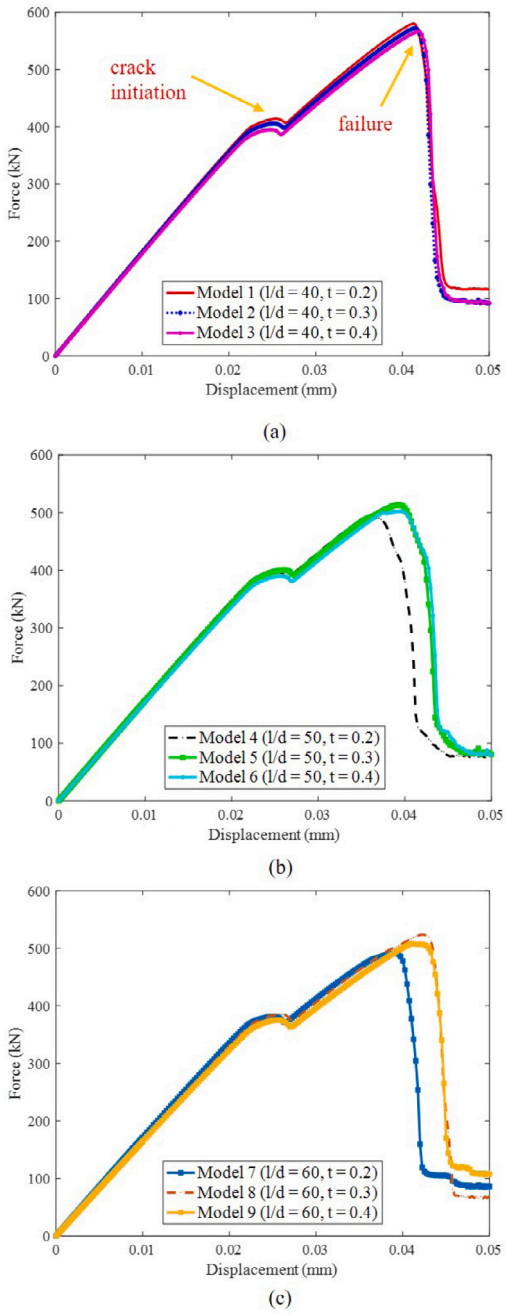

Fig. 6. Force–displacement results of MFRCs under tension (polyester fiber) (a) models 1–3, (b) models 4–6, (c) models 7–9. Model 1 shows the highest peak force. However, excluding this model, it can be seen that the shell thickness = 0.3 mm can improve the peak force compared to 0.2 and 0.4 mm.

Table 5
Normalized values of energy absorption and peak force of MFRCs under compression. Model 1 exhibits the highest W_{tot} (939.67 J), W_{py} (773.79), and PF (5639.20 kN).

Model No.	W_{tot} (J)	W_{py} (J)	PF (kN)
Model 1	1	1	1
Model 2	0.975002	0.975239	0.974887
Model 3	0.950025	0.950439	0.950968
Model 4	0.920791	0.920327	0.930134
Model 5	0.891685	0.891573	0.900009
Model 6	0.863527	0.863852	0.871987
Model 7	0.847702	0.847	0.860966
Model 8	0.815882	0.815777	0.832072
Model 9	0.785584	0.785846	0.800954

which is the second highest in terms of absorbed energy), it can be concluded that under three-point bending, higher shell thickness can result in higher energy absorption, whereas it is the lowest l/d ratio (40) which results in higher peak forces.

3.4. Material mismatch effects on the mechanical response of MFRCs

Like explained in Section 2.2, one purpose of the study is to look into the performance of MFRCs considering the different material mismatch effects. To do so, different material property mismatches for the shell are considered (Table 2).

3.4.1. Fracture response of MFRCs under tension

The normalized results of the MFRC models under tension for different material sets have been exhibited in Table 7. In order to focus

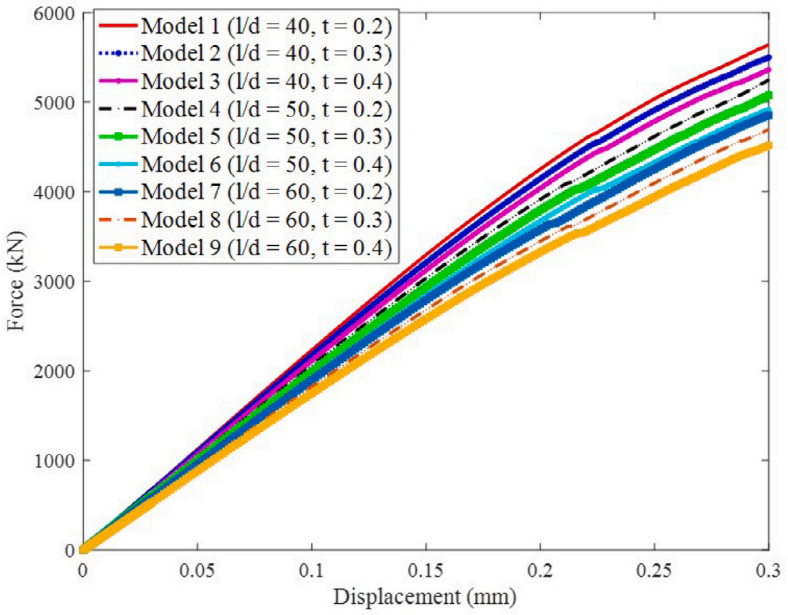

Fig. 7. Force–displacement results of MFRCs under compression. With an increase in l/d ratio and t, peak force and energy absorption slightly decrease.

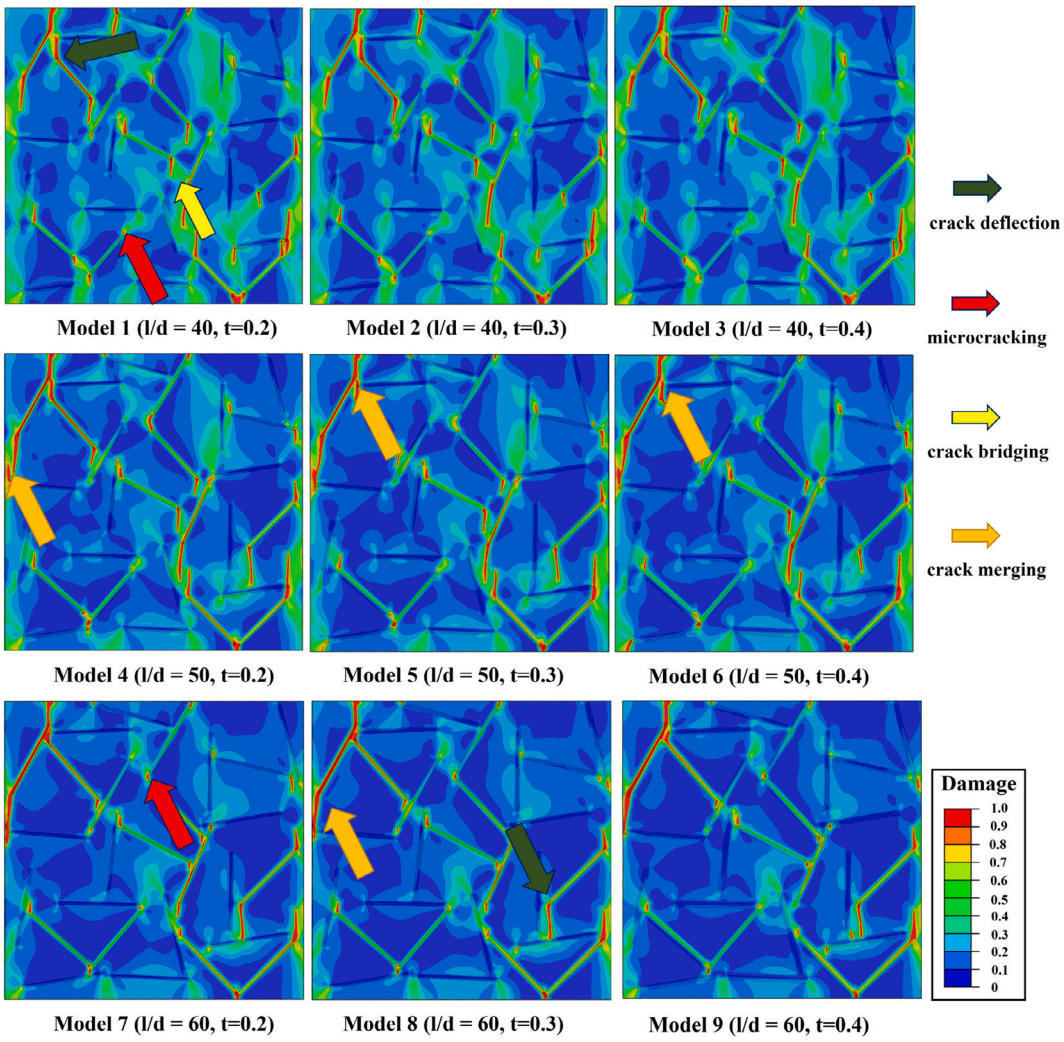

Fig. 8. The crack propagation in MFRCs under compression. Different toughening mechanisms are shown in several models. Microcracking, crack bridging and crack deflection is shown in model 1, as an example, which is beneficial for its overall fracture response.

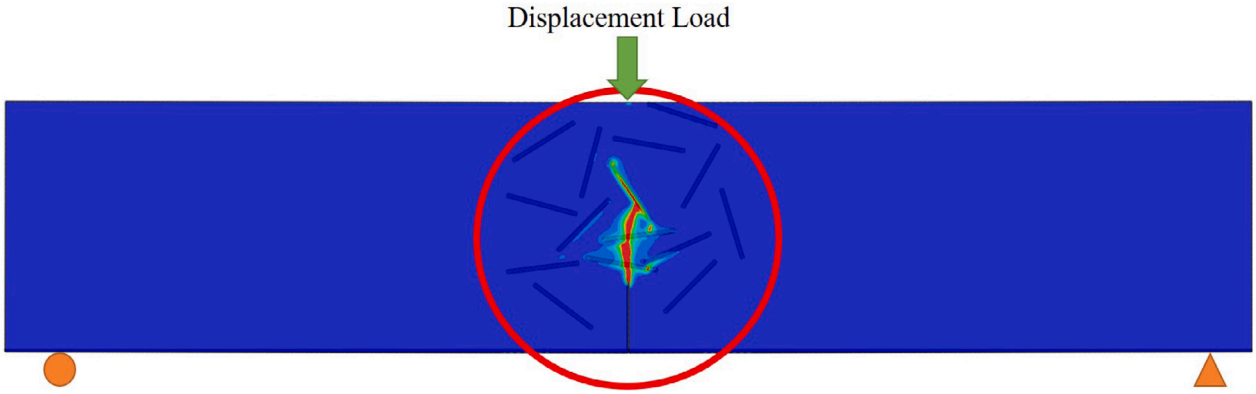

Fig. 9. Setup of MFRCs under three-point bending loading.

Table 6
Energy absorption and peak force of the MFRCs under three-point bending. The highest energy absorption and peak force are shown by model 3 and model 2, respectively.

Model No.	W_{tot} (J)	W_{py} (J)	PF (kN)
Model 1	0.918052	0.889855	0.995546
Model 2	0.938242	0.92029	1
Model 3	1	1	0.985345
Model 4	0.796912	0.750725	0.849425
Model 5	0.833729	0.802899	0.883333
Model 6	0.964371	0.966667	0.958908
Model 7	0.817102	0.788406	0.800431
Model 8	0.832542	0.814493	0.804023
Model 9	0.814727	0.8	0.796121

on the effect of the material mismatch on the fracture response of the structures, prior to choosing the model with the most favorable result for each material set, the results of specific models with different material sets will be considered and compared. When taken model 1 as a case study, it can be seen that as we move from material set 1 (tougher shell) to material set 2 (average tough shell) and 3 (less tough shell), the amount of absorbed energy and peak force decreases. This reduction in the values of total absorbed energy and peak force can be seen for all models when the results of the material sets 1 to 3 are compared for any specific model.

When all models in each material set are considered and reviewed carefully, for the material sets 2 and 3, similar to the material set 1, model 1 shows a favorable response as it has the highest energy absorption and peak force in comparison with those of other models under tension. However, regarding the material set 4, which has a fiber with higher critical energy release rate (polypropylene), the choice of the model with most favorable performance can be more tough. In this set, there are two outstanding models, one showing the highest energy absorption and the other having the highest peak force.

In order to have a means of comparison, we can define the relation below in order to obtain a normalized magnitude for these models:

$$Overall\ Performance = (Peak\ Force)/(Max.\ Peak\ Force) + (Energy\ Absorption)/(Max.\ Energy\ Absorption) \quad (11)$$

where

$$Overall\ Performance \leq 2$$

Based on Eq. (11), for the material set 4, model 6 and model 9 have overall performances of 1.959 and 1.977. Consequently, model 9 has the most favorable mechanical response.

The crack propagation for these models under tension has been exhibited in Fig. 12. In the case of material set 4, due to a much higher critical energy release rate of the polypropylene fiber, the fibers are almost intact and the crack propagates through the shell and the concrete (Fig. 12c). Moreover, like it can be checked in Fig. 13, the models with polypropylene fibers fail at higher displacement loads compared to polyester fibers, resulting in higher energy absorption capacity and peak force.

For the record, the values of W_{tot}, W_{py}, and PF in material set 2 for model 1 are 15.68 J, 11.27 J, 570.43 kN, respectively. In material set 3, these values are 14.98 J, 10.58 J, and 554.57 kN for model 1. For material set 4, W_{tot} and W_{py} of model 9 are 22.97 J and 18.59 J, respectively, while the highest peak force with the value of 681.50 kN was displayed by model 6.

3.4.2. Fracture response of MFRCs under compression

The normalized results of all MFRCs with different material sets under compression can be checked in Table 8. When the results of any model is checked considering different material sets, it can be realized that the less tough the shell is, the less peak force is withstood and less energy is absorbed. However, the results are very close and comparable to each other for the material sets 1 to 3, where the critical energy release rate of the shell changes. Nevertheless, for material set 4 (tough

Table 7
The normalized results of the MFRCs under tension with different material sets. Model 1 shows the most favorable result with material sets 2 (average tough shell) and 3 (less tough shell) similar to set 1 (tough shell). Regarding material set 4 (tough fiber), there are 2 models in each that have the most favorable fracture response. The highest peak force and energy absorption values in each material set have been highlighted in gray for convenience.

Model No.	*Material set* 1			*Material set* 2			*Material set* 3			*Material set* 4		
	W_{tot} (J)	W_{py} (J)	PF (kN)	W_{tot} (J)	W_{py} (J)	PF (kN)	W_{tot} (J)	W_{py} (J)	PF (kN)	W_{tot} (J)	W_{py} (J)	PF (kN)
1	1	1	1	1	1	1	1	1	1	0.793209	0.727273	0.923096
2	0.970678	0.964617	0.985937	0.969388	0.963696	0.975615	0.962617	0.953686	0.971059	0.811929	0.754169	0.937212
3	0.971289	0.971356	0.976148	0.95727	0.951106	0.964045	0.943925	0.931947	0.95355	0.845451	0.799354	0.948966
4	0.854001	0.812131	0.844857	0.859694	0.806543	0.8299	0.841121	0.789225	0.822619	0.827601	0.772458	0.912707
5	0.917532	0.905644	0.884737	0.944515	0.884658	0.862647	0.883178	0.855388	0.845718	0.966913	0.949435	0.982377
6	0.910812	0.902275	0.865556	0.892219	0.875719	0.841681	0.867156	0.840265	0.822691	0.959948	0.94567	1
7	0.859499	0.83235	0.84727	0.853316	0.824312	0.832127	0.845794	0.810019	0.821159	0.831955	0.781065	0.900249
8	0.924863	0.928391	0.902351	0.907526	0.905945	0.877443	0.890521	0.880907	0.859116	0.959948	0.944594	0.966368
9	0.932804	0.946083	0.875241	0.906888	0.912156	0.850551	0.875834	0.86673	0.829796	1	1	0.977623

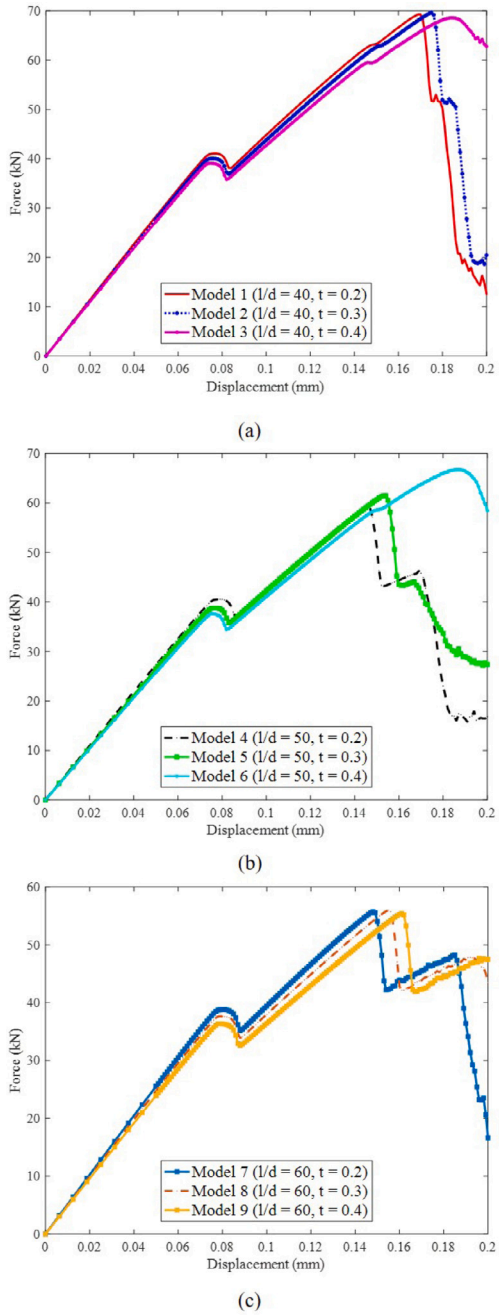

Fig. 10. Force–displacement results of the MFRCs under three-point bending (a) models 1–3, (b) models 4–6, (c) models 7–9. MFRC models with $l/d = 40$ (models 1–3) show better fracture response. The re-hardening phenomenon happening due to the presence of fibers after the yielding of concrete also increases the strength of the structure.

fiber), there is a significant increase in both the amount of absorbed energy and the peak force that the structure can undergo.

In order to choose the most favorable structure in each material set, unlike tension, under compression, as it can be checked, model 1 has displayed the most favorable performance in terms of both absorbed energy and peak force compared to other models for different material sets. The force–displacement results of the blocks with different material sets can also be checked in Fig. 14. This figure confirms the higher energy absorption and peak forces of the models with polypropylene fiber (material set 4). The less tough shell material (material set 3) has also resulted in the least efficient mechanical response (Fig. 14b). In order to have means of comparison, Fig. 15 shows the crack propagation under compressive loading for model 1 with material sets 1 and 4.

To be able to compare the results of model 1 with different material sets, the values of W_{tot}, W_{py}, and PF in material set 2 are 938.39 J, 771.32 J, 5632.10 kN, respectively. These values, in the same order, change to 936.97 J, 771.12 J, 5625.52 kN in material set 3. However, in material set 4, they considerably increase to 1115.717 J, 922.58 J, 6871.77 kN, respectively.

3.4.3. Fracture response of MFRCs under three-point bending

The normalized results of the MFRC models under three-point bending can be seen in Table 9. The force–displacement results of MFRCs with different material sets under three-point bending have been tabulated in Fig. 16 for a further comparison of the mechanical response of the models as well. When the results of different models with different material sets are considered, it can be understood that for all models, the material set 3 has rendered a higher energy absorption capacity. For instance, in the case of model 1, even though by the use of less tough

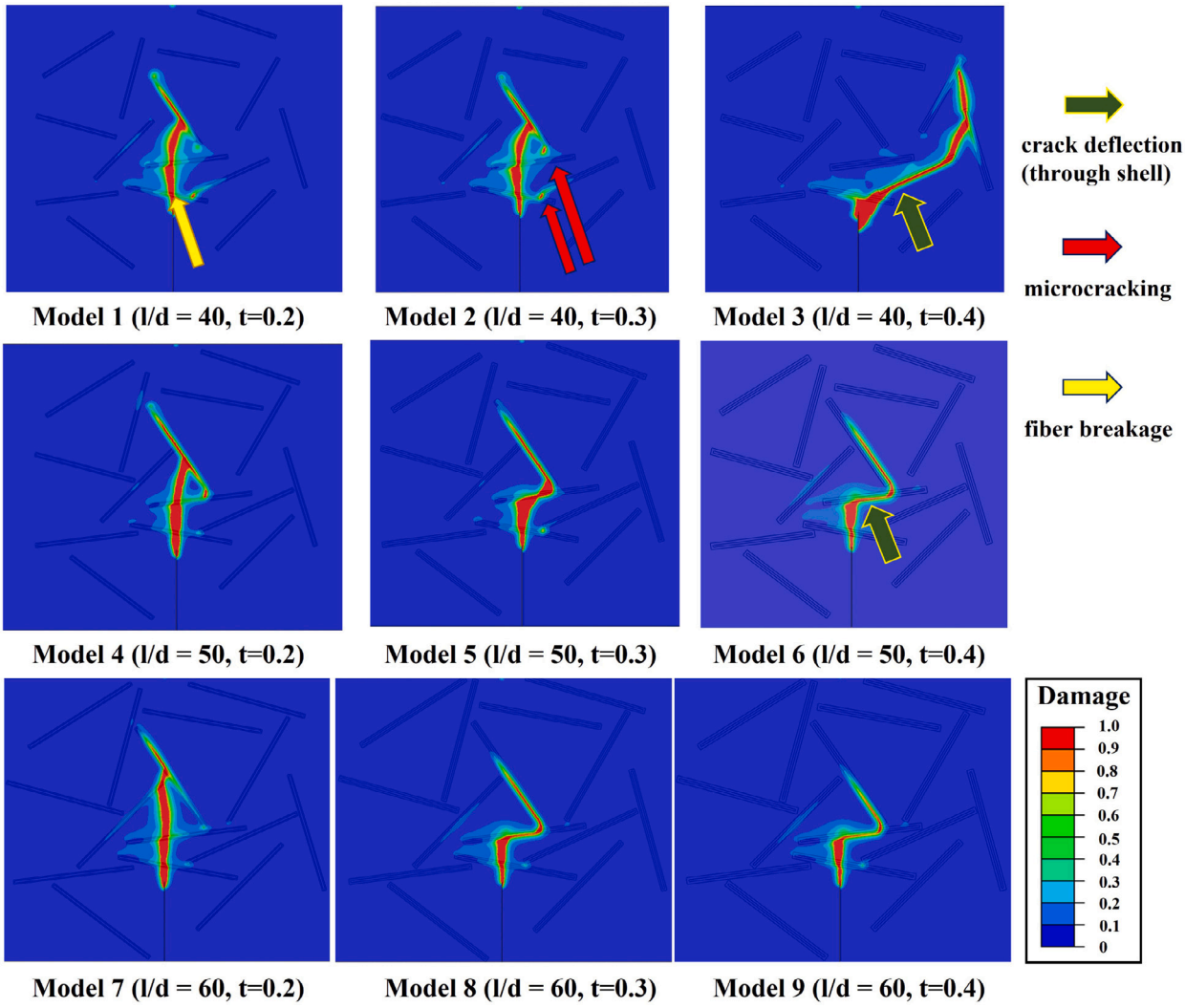

Fig. 11. The crack propagation in the MFRCs under three-point bending. The microcracking and crack deflection in models 2 and 3 have contributed to a higher peak force and energy absorption, respectively.

Table 8
The results of the MFRCs under compression with different material sets. Model 1 shows the most favorable mechanical response in all material sets. The highest peak force and energy absorption values in each material set have been highlighted in gray for convenience.

Model No.	*Material set* 1			*Material set* 2			*Material set* 3			*Material set* 4		
	W_{tot} (J)	W_{py} (J)	PF (kN)	W_{tot} (J)	W_{py} (J)	PF (kN)	W_{tot} (J)	W_{py} (J)	PF (kN)	W_{tot} (J)	W_{py} (J)	PF (kN)
1	1	1	1	1	1	1	1	1	1	1	1	1
2	0.975002	0.975239	0.974887	0.974627	0.974278	0.973303	0.974065	0.974116	0.972154	0.9652	0.96564	0.96765
3	0.950025	0.950439	0.950968	0.949488	0.952458	0.948657	0.948216	0.948283	0.945454	0.932226	0.932559	0.935513
4	0.920791	0.920327	0.930134	0.919777	0.920707	0.929069	0.91972	0.919079	0.927655	0.975857	0.976815	0.981974
5	0.891685	0.891573	0.900009	0.889907	0.891135	0.897644	0.889335	0.888811	0.895645	0.933427	0.93451	0.942452
6	0.863527	0.863852	0.871987	0.861433	0.863286	0.866712	0.859846	0.859477	0.863392	0.893327	0.894361	0.902802
7	0.847702	0.847	0.860966	0.847153	0.847003	0.859234	0.845609	0.844629	0.855501	0.952948	0.95466	0.965556
8	0.815882	0.815777	0.832072	0.814224	0.81625	0.828547	0.812587	0.811936	0.826702	0.902666	0.904399	0.916842
9	0.785584	0.785846	0.800954	0.78331	0.785044	0.797354	0.780943	0.780384	0.78834	0.856239	0.857833	0.87038

shell (material set 3) the peak force slightly decreases from 69.29 to 67.24 kN, the total energy absorption increases by 30%, from 7.73 to 10.05 J. These results also indicate that for the polypropylene fiber (the material set 4), the flexural strength increases with an increase in the fiber length.

As it can be checked, choosing the most favorable model with the material sets 1 (tough shell) and 2 (average tough shell) under this loading condition is not as straightforward as the compression loading type. In each of these material sets, two models stand out, one having the highest absorbed energy and the other the highest peak force. Nevertheless, it can be seen that for the material sets 3 and 4, model 1 and model 6 show the most favorable performance, respectively. To determine the most favorable models for material sets 1 and 2, a similar approach to tension results in Section 3.4.1 will be chosen to determine the overall performance.

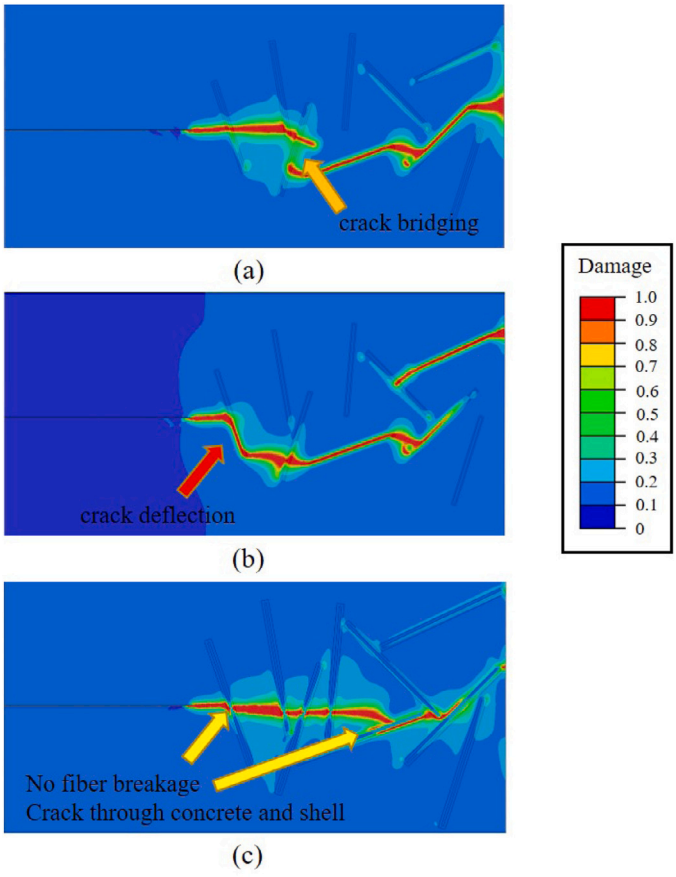

Fig. 12. Crack propagation through MFRCs with the best overall response under tension (a) Model 1 with the material set 2, (b) Model 1 with the material set 3, (c) Model 9 with the material set 4. Crack bridging, deflection, and no fiber breakage in each of these models have played a vital role in having more favorable results.

Table 9
The normalized results of the MFRCs under three-point bending with different material sets. Model 1 shows the most favorable result with material sets 2 (average tough shell) and 3 (less tough shell) similar to set 1 (tough shell). Regarding material set 4 (tough fiber), there are 2 models in each that have the most favorable fracture response. The highest peak force and energy absorption values in each material set have been highlighted in gray for convenience.

Model No.	*Material set* 1			*Material set* 2			*Material set* 3			*Material set* 4		
	W_{tot} (J)	W_{py} (J)	PF (kN)	W_{tot} (J)	W_{py} (J)	PF (kN)	W_{tot} (J)	W_{py} (J)	PF (kN)	W_{tot} (J)	W_{py} (J)	PF (kN)
1	0.918052	0.889855	0.995546	0.956704	0.923623	0.994423	1	1	1	0.889746	0.850267	0.969648
2	0.938242	0.92029	1	0.98324	0.957371	1	0.971144	0.969267	0.97561	0.949283	0.926471	0.986992
3	1	1	0.985345	0.96648	0.937833	0.986385	0.940299	0.937352	0.916568	0.988975	0.981283	0.996612
4	0.796912	0.750725	0.849425	0.959497	0.936057	0.953576	0.770149	0.735225	0.874926	0.929438	0.90107	0.943767
5	0.833729	0.802899	0.883333	0.973464	0.955595	0.977034	0.925373	0.92435	0.909726	0.954796	0.938503	0.979268
6	0.964371	0.966667	0.958908	0.980447	0.9627	0.981627	0.902488	0.901891	0.895152	1	1	1
7	0.817102	0.788406	0.800431	0.993017	0.992895	0.91601	0.821891	0.807329	0.818412	0.897464	0.86631	0.92561
8	0.832542	0.814493	0.804023	1	1	0.920932	0.848756	0.845154	0.877008	0.92613	0.910428	0.930894
9	0.814727	0.8	0.796121	0.997207	0.996448	0.92044	0.842786	0.84279	0.873736	0.980154	0.983957	0.938889

Based on Eq. (11), it can be seen that among MFRCs of the material set 1, model 2 and model 3 have an overall performance of 1.938 and 1.985, respectively, signifying that model 3 (l/d = 40, t = 0.4) has the most favorable response with this material set under three-point bending. For model 2 and model 8 with the material set 2, the overall performances are 1.983 and 1.920, respectively. Therefore, for this material set, the most favorable response is for model 2 (l/d = 40, t = 0.3). Crack propagation in the outstanding models in each material set can be checked in Fig. 17.

As a reference, in material set 2, the maximum values of W_{tot} and W_{py} were shown by model 8 (7.16 J and 5.63 J, in the same order). However, the maximum PF was for model 1 (60.96 kN). In the case of material set 3, the highest values of W_{tot}, W_{py}, and PF were seen by model 1 (10.05 J, 8.46 J, and 67.24 kN, respectively). For material set 4, model 6 displayed the highest W_{tot}, W_{py}, and PF, which were 9.07 J, 7.48 J, and 73.80 kN, respectively.

3.5. 3D simulation of crack in MFRCs under tension

The finite element models of 3D MFRCs have already been explained and exhibited in Fig. 3. Their force–displacement results under tensile loading can be checked in Fig. 18. The crack propagation in these two models have also been exhibited in Fig. 19.

As it can be seen, in the model with perpendicular fibers, the amount of PF that the block underwent is considerably higher than of the other one. This is expected as the fibers in this model are in the direction of loading. This results in a higher elastic response and ultimately a rise in the PF. For a more in-detail investigation, the PFs and values of W_{tot} and W_{py} for these two models can be checked in Table 10. Like it can be checked, when fibers are placed perpendicularly with respect to the pre-crack, W_{tot}, W_{py}, and PF increase by almost 58%, 44% and 54%, respectively.

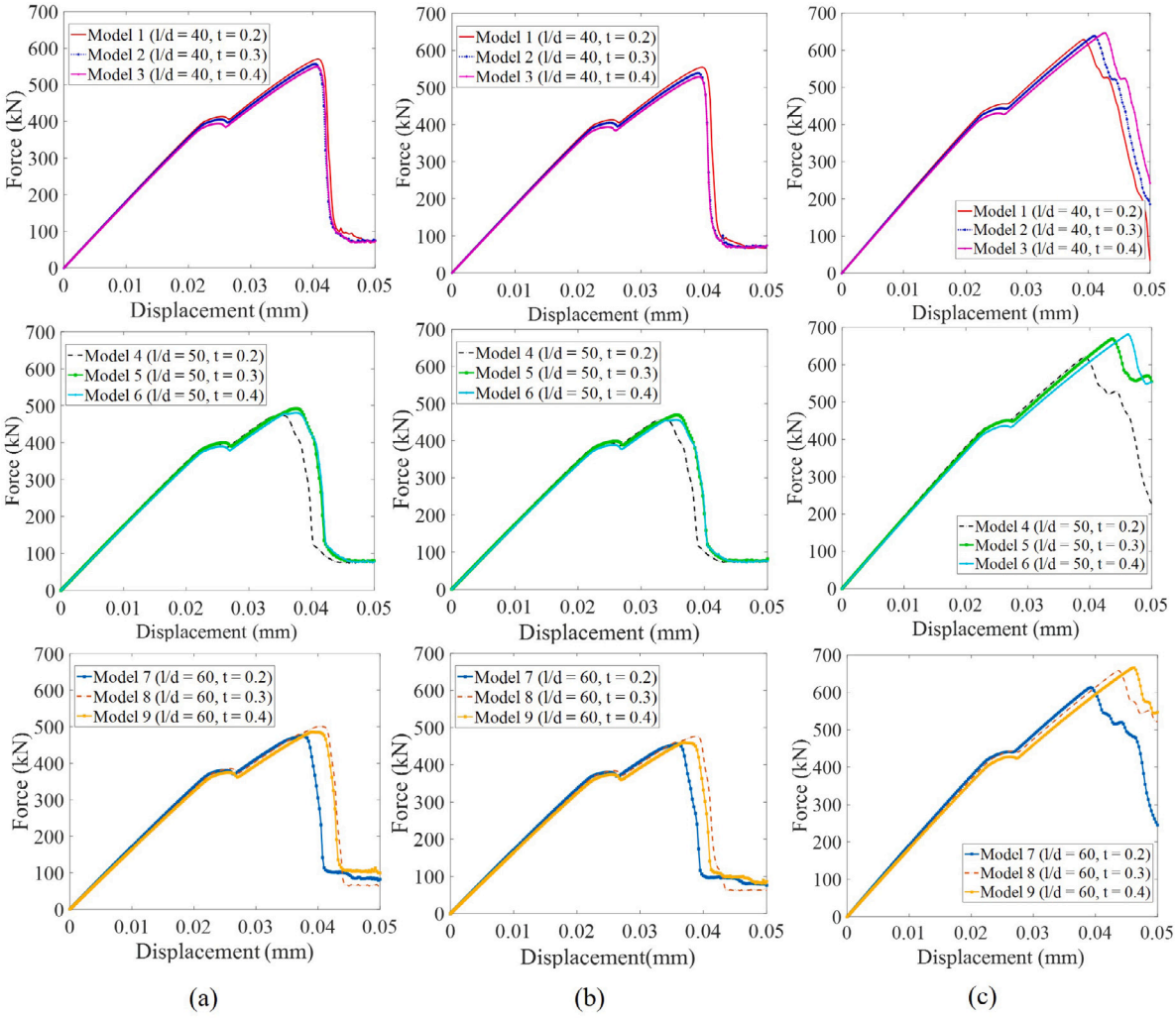

Fig. 13. Force–displacement results of the MFRCs with different material sets under tension (a) Material set 2, (b) Material set 3, (c) Material set 4. With a lower G_{Shell} than of the matrix (material set 3), we can see a drop in the mechanical response for material set 3. In material set 4, due to a much tougher fiber (polypropylene), results are much more favorable.

Table 10
The results of the 3D MFRC models under tension. Perpendicular fibers resulted in a far more favorable fracture response.

	W_{tot} (J)	W_{py} (J)	PF (kN)
Anti-parallel fibers	170.89	149.41	5.73
Perpendicular fibers	243.52	214.97	8.80

Table 11
The comparison of the results of the 3D MFRC models under tension with different fibers. More favorable fracture response resulted from the utilization of polypropylene fiber.

	W_{tot} (J)	W_{py} (J)	PF (kN)
Polyester fiber	243.52	214.97	8.34
Polypropylene fiber	284.11	247.66	10.06

Additionally, in order to have a better understanding of the fracture response of concrete blocks with polypropylene fiber and compare them with polyester fibers, the 3D MFRC model with perpendicular fibers were restudied with the material property of the polypropylene fiber. The force–displacement results can be looked into in Fig. 20.

As it can be seen in Fig. 20, when polypropylene fiber is utilized, there is a tangible increase in the amount of peak force. This is partly owing to the fact that the higher critical energy release rate of polypropylene fiber than of polypropylene, increases the toughness of the whole structure. Table 11 can be used for a more in-depth analysis of the impact of the polypropylene fiber on the mechanical response of MFRCs.

Fig. 21 also shows the crack propagation in the 3D MFRCs with polyester and polypropylene fibers placed perpendicularly to the pre-crack for further comparison.

To compare the fracture response of the microstructures of MFRCs more in-depth and have a better understanding of the effect of alignment of the fibers in anti-parallel and perpendicular planes with respect to the pre-crack on the fracture response, the effective crack growth resistance of these microstructures (G_I) have been evaluated below[1]:(ASTM-D5528, 2007; Hashemi et al., 1989; Shokrieh et al., 2012; Beaumont et al., 2015; Prasad et al., 2011):

$$G_I = \frac{3P_c\delta}{2b(a+\Delta)} \tag{12}$$

[1] This relation was developed to obtain the fracture energy (crack growth resistance) through the single-edge tensile test of laminated composites as it can be checked in the references.

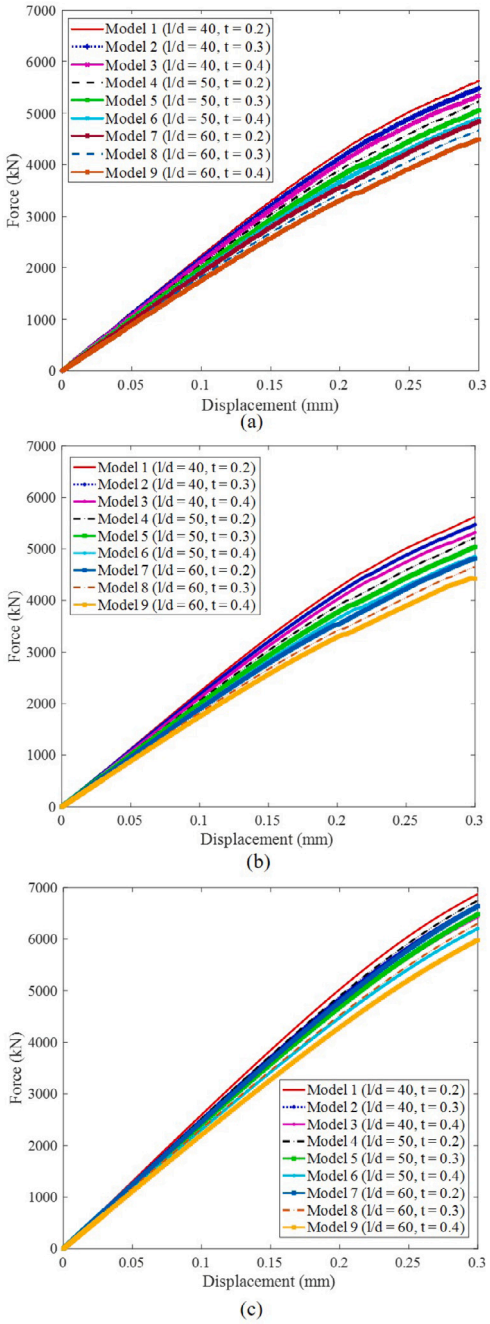

Fig. 14. Force–displacement results of the MFRCs with different material sets under compression (a) Material set 2, (b) Material set 3, (c) Material set 4. With a rise in l/d and t, there is a slight drop for all material sets in energy absorption and peak force.

where P_c is the load at which the crack propagates, δ is the displacement at the load point, b is the sample width, a is the crack length, and Δ is the correction factor added to the equation above due to possibility of rotation which may occur at the delamination front. However, since the tensile loads imposed on FEMs have been prescribed only in Y-direction and rotations have been restrained, this factor can be disregarded. Hence, the equation can be regarded as:

$$G_I = \frac{3P_c\delta}{2ab} \tag{13}$$

Based on the equation above, the effective crack growth of the microstructures of MFRC are determined as Table 12:

Table 12
The effective crack growth resistance of the MFRC microstructures with different fibers and alignments.

Fiber - Alignment	G_I (kJ/m^2)
Polyester - Anti-parallel	1.232379808
Polyester - Perpendicular	1.756153846
Polypropylene - Perpendicular	2.048870192

As it can be seen, the effective crack growth resistance of the perpendicular alignment of polyester is almost 42% higher than that of anti-parallel one. Moreover, by the use of polypropylene fibers, this value increases by about 17%.

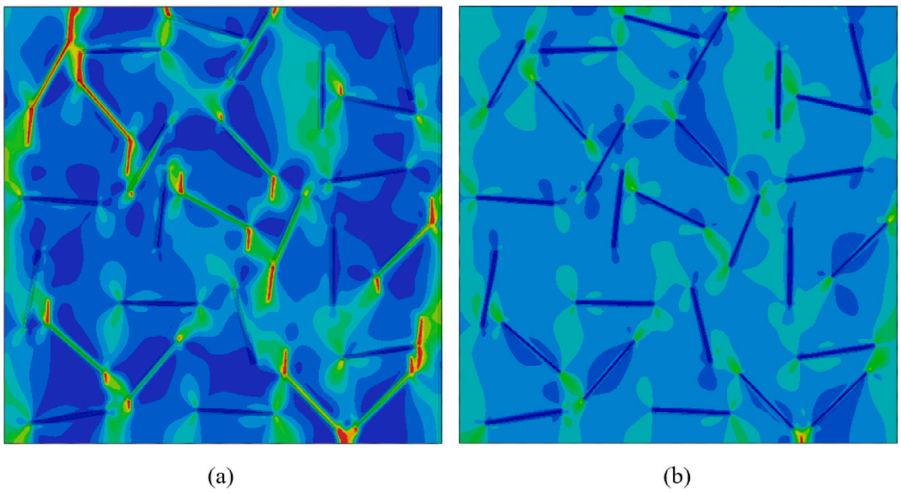

Fig. 15. Crack propagation through the MFRCs with the best overall response under compression (a) model 1 with the material set 1 (polyester fiber), (b) model 1 with the material set 4 (polypropylene fiber). By using the tougher fiber (material set 4), partial damage and microcracking contributes to energy absorption while, in the same displacement load step, crack propagates in MFRCs with other material sets.

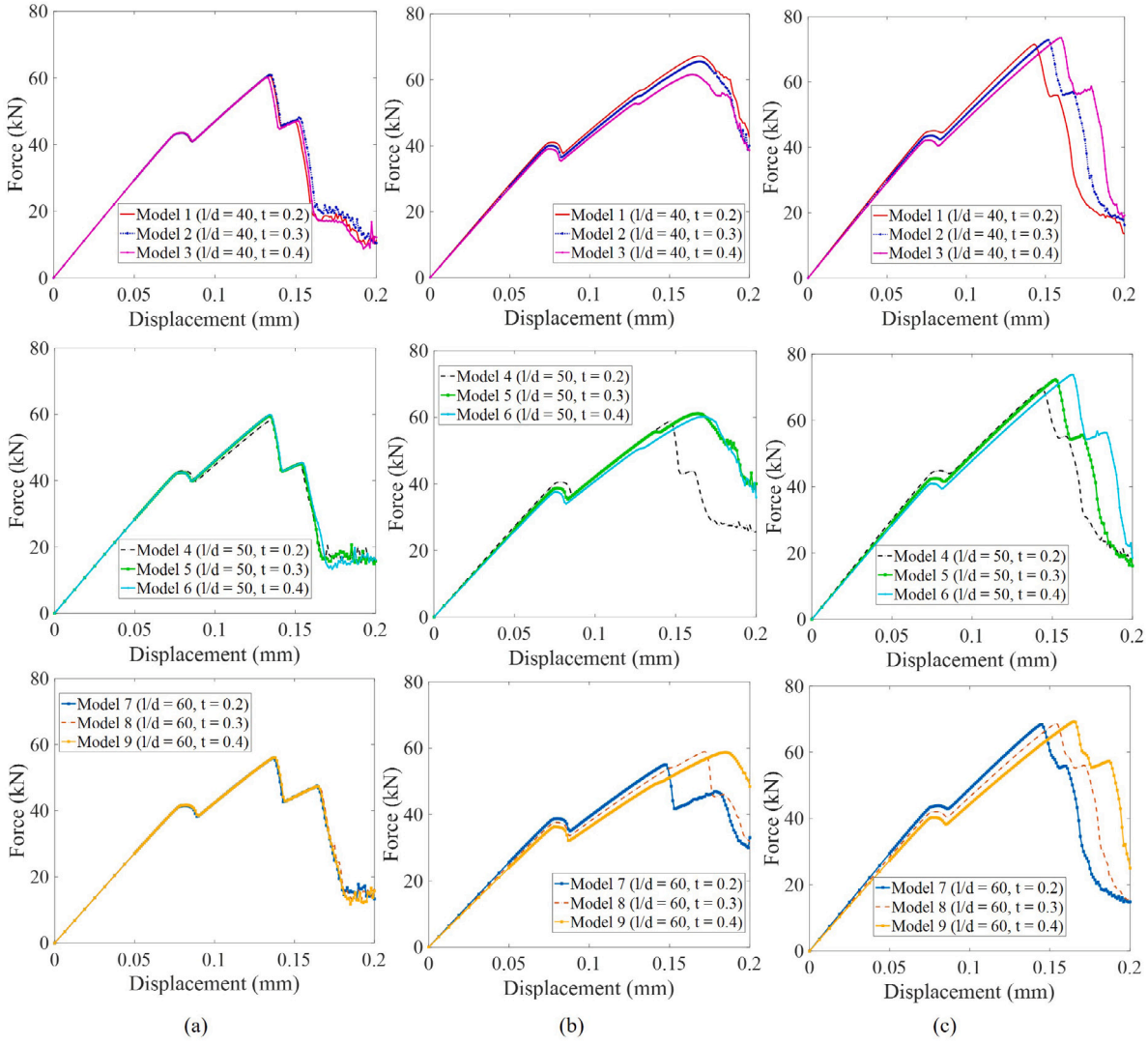

Fig. 16. Force–displacement results of MFRCs with different material sets under three-point bending (a) Material set 2, (b) Material set 3, (c) Material set 4. Under three-point bending, results for material set 2 are almost independent from t. For the material set 3, there is a slight drop in the peak force of MFRCs. However, the absorbed energy is higher due to the debonding of the fibers. In the material set 4, tougher fiber contributes to considerably higher peak force and energy absorption (compared to the results of the material set 1).

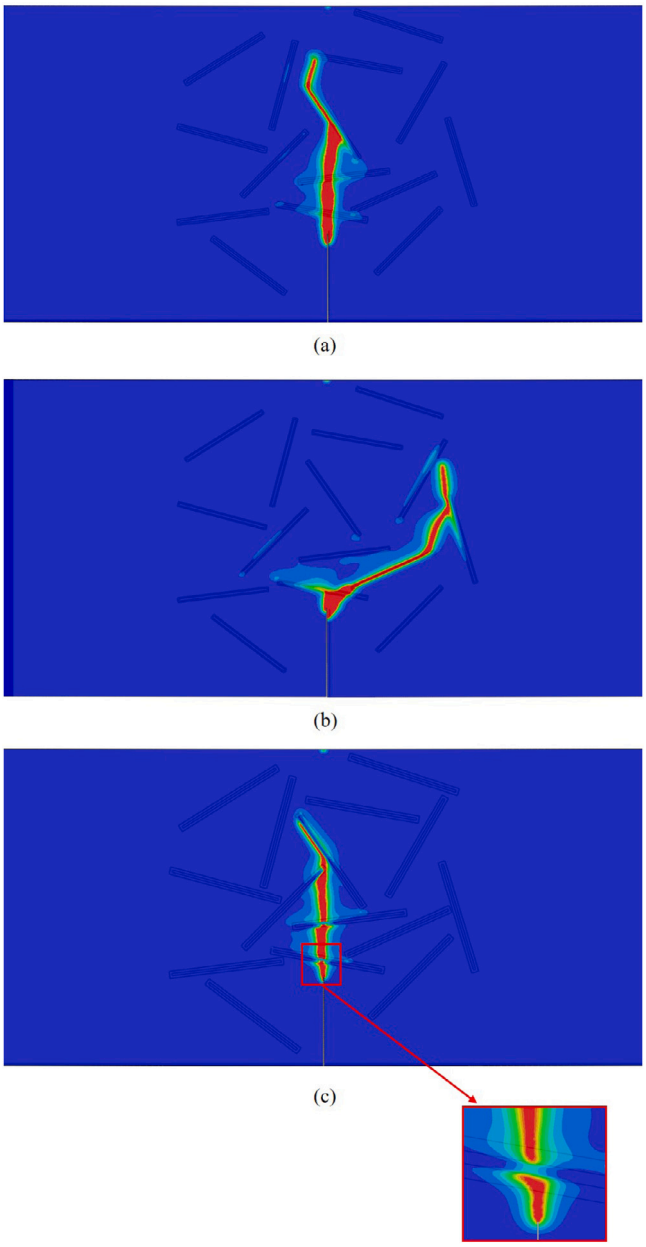

Fig. 17. Crack propagation through the MFRCs with the best overall response under three-point bending (a) model 2 with the material set 2, (b) model 1 with the material set 3, (c) model 6 with the material set 4. Microcracking (a), crack deflection (b), and no fiber breakage (c) are observed.

4. Discussion

4.1. On the results of MFRCs under tensile loading

With a look at the results of MFRCs under tensile loading in Section 3.1, it was understood that the models with lower l/d values have a higher peak force at the early stages of crack propagation and can undergo higher tensile displacement loads until failed. A reasonable justification is that the higher l/d values, *i.e.* higher volume fraction (as the surface area of the models and number of fibers are fixed), cause the fibers to be more densely placed in a given area. With the fibers densely placed close to each other, the interactive effect between the fibers stronger, resulting in their stress fields to impact that of one another. Consequently, the crack merging and failure of the structure happen at a lower displacement load. Moreover, based on Fig. 5, in model 1, the most favorable response can be put down to several crack deflections that happen, along with the crack bridging. Although these toughening mechanisms can be seen in other models as well, they are not as dominant as of model 1. For instance, in the case of model 9, crack bridging can be observed, however, not as dominant. The result of this section is in agreement with previous research (Khan et al., 2021), where different lengths of polyester fiber were used to reinforce concrete (12, 25, 37, 50 mm). The results showed with a low content of fibers (0.45%–1%), 12-mm fibers increased fracture resistance more effectively.

In Section 3.4.1, it was also seen MFRCs with material sets 2 (average tough shell) and 3 (less tough shell), the fracture response of MFRCs deteriorates. This can be attributed to the fact that utilizing a shell material with lower critical energy release rate can result in faster crack propagation and crack merging through the structure. This in turn results in the instability of the structure and reaching failure faster and more easily. In the case of material set 4, a much better mechanical response for all models was observed under tension. This stems from the fact that due to a much higher critical energy release

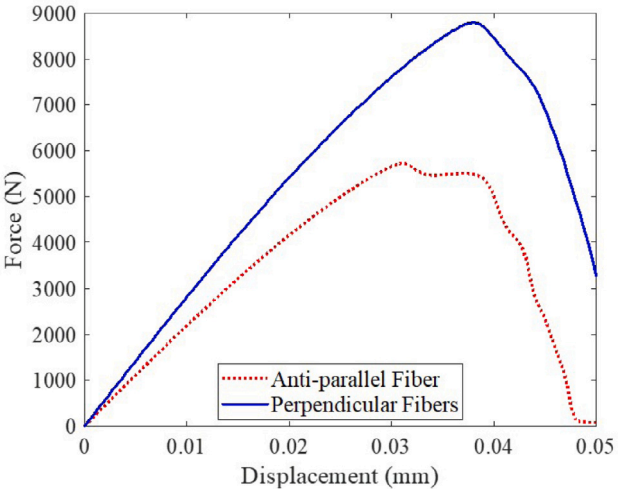

Fig. 18. The force–displacement results of the 3D MFRC models under tension. Model with perpendicular fibers show a slightly higher peak force and energy absorption.

rate of the polypropylene fiber, the fibers are almost intact and the crack propagates through the shell and the concrete (Fig. 12c). It was also shown that among the models with the material set 4, models 6 and 9 exhibit the highest peak force and energy absorption, respectively. Our assumption is that as the fibers are much tougher and are left intact, the crack tends to propagate through the shell. The highest shell thickness enables the crack to more smoothly propagate through the interface, which causes the fiber to debond from the concrete and absorb more energy.

The results in this section are also in agreement with other studies. For the tougher fibers (polypropylene), an increase in the fiber length can effectively increase the fracture energy of the structure. The same conclusion was made in studies done by Bencardino et al. (2010), Yoo et al. (2015b), Han et al. (2019) and Sovják et al. (2017), where the tensile strength of the concrete increases with an increase in polypropylene fiber length. In terms of material mismatch effects of the fiber type, other researches report the same results as the present study. Koniki and Prasad (2019) showed that compared to polyester fiber reinforced concrete, addition of polypropylene fiber can more effectively improve the energy absorption and fracture resistance of the concrete. Another work also suggested that polypropylene fiber reinforced concrete exhibit higher crack resistance and tensile strength (Rostami et al., 2019).

4.2. On the results of MFRCs under compressive loading

As it can be looked into Fig. 8, the higher energy absorption and peak force for the models with lower l/d ratio and shell thickness can be attributed to the fact that the damage is more evenly distributed within the matrix (concrete) for these models. This means that the structure absorbs more energy through several partial damage ($d < 1$) before reaching complete failure through crack merging. Moreover, Fig. 8 suggests that thinner shell thickness cause the cracks to propagate through the shells slightly more smoothly, which makes the fiber and concrete debonding happen. Consequently, a slightly better toughness, energy absorption capacity and peak force can be achieved. Furthermore, with a look at model 1, we can see that the toughening mechanisms are microcracking and crack deflection. Additionally, crack bridging can be observed to be more dominant for models with lower l/d (shown in model 1), compared with models with longer fibers (for instance model 9). In models with higher l/d ratio (for instance model 8), cracks merge at the top of the model, leading to MFRCs failure. Similar findings have been reported in other researches (Han et al., 2019) and Yoo et al. (2014). They proposed that the addition of longer fibers does not improve the compressive response. This can be attributed to the fact that longer fibers do not provide higher compressive strength due to fiber buckling or bending.

As different material sets were considered for MFRCs under compressive loading (Section 3.4.2), models with the lowest l/d ratio and shell thickness consistently confirmed the best fracture response. The results for material sets 1–3 were pretty close. However, MFRCs with polypropylene fiber showed much better fracture response under compressive loading. Fig. 15 could explain the underlying reason for this observation. As it can be observed, at the same value of displacement load that model 1 with the material set 1 undergoes crack initiation and crack propagation, the energy has been efficiently dissipated by using polypropylene fibers throughout the whole structure, constraining the crack propagation and failure of the structure. In line with previous research, a hybrid polyester fiber reinforced concrete displays higher energy absorption compared to steel fiber reinforced concrete (Chella Gifta and Prabavathy, 2018). Nonetheless, similar to our findings, polypropylene fibers was found to more effectively increase the compressive strength of fiber reinforced concrete among other non-metallic fibers (Bolat et al., 2014). Koniki and Prasad (2019) also worked on non-metallic fiber reinforced concrete, and suggested than under compression, addition of polypropylene fiber can increase the absorbed energy of the fiber reinforced concrete more beneficially than if polyester fiber reinforced concrete is used.

4.3. On the results of MFRCs under three-point bending

Table 6 showed that MFRCs with lower l/d ratios also exhibit better fracture response under three-point bending. However, the highest

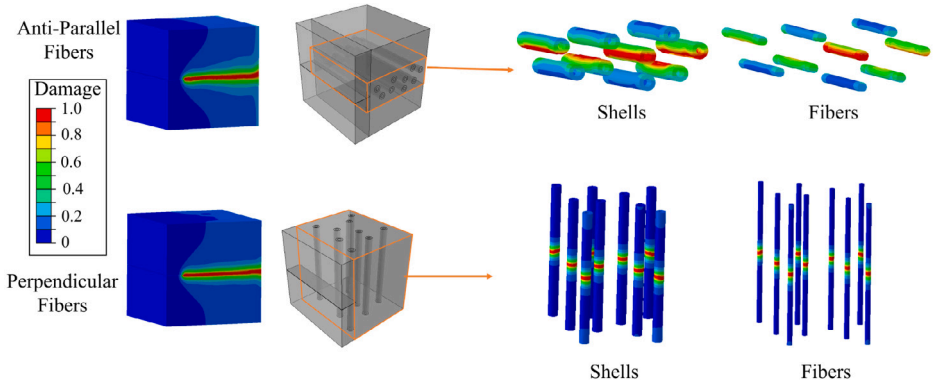

Fig. 19. The crack propagation through MFRC with the anti-parallel fibers and the perpendicular fibers. For the anti-parallel model, some fibers and shells remain intact while for the other, all contribute to the fracture response.

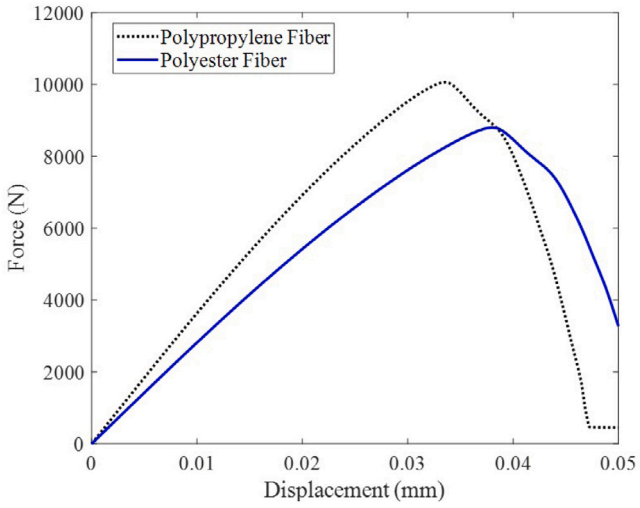

Fig. 20. The force–displacement results of the 3D MFRC models under tension with different fibers. Higher peak force and energy absorption can be seen by using a tougher fiber.

energy absorption is by the Models 3 and 6 with the highest shell thickness. The higher magnitude of energy absorption for the two models 3 and 6 stems from the crack deflection and propagation through the shell that can be seen in Fig. 11. Crack propagation through shell causes the interface to fail (fiber debonds from the concrete), and accordingly more energy can be absorbed. A considerable crack deflection can be seen for model 3, as it propagates through the concrete and shell mostly and breaks only one fiber. This observation, which has lead to a high energy absorption, cannot be seen in other models, however. For model 6, a slight crack deflection can be seen, while for other models (like model 1 and 2), crack breaks the fibers and propagates without any deflection. For models 1 and 2, though, crack deflection is minor, and microcracks and fiber breakage can be seen, which both have contributed to a slightly better peak force. However, the less post-yielding absorbed energy for these two models result in an overall lower total energy absorption.

Another observation in Fig. 10 that can justify the results is the re-hardening phenomenon in MFRCs under three-point bending. After the concrete is damaged, the crack reaches the fibers, which stop it from propagation. However, with a rise in the displacement load, the crack is either deflected through the shell or continues propagating through the fibers. This causes several re-hardenings occur before the complete failure of MFRCs, which in turn increases their strength. These re-hardening observations are predominant for the cases with higher shell thickness ($t = 0.4$).

The results observed in Section 3.3 are in agreement with other studies. In a study done on fiber reinforced concretes to investigate the effect of fiber length on flexural strength of the structure, it was seen that when fibers are about the length of 14 mm, compared to longer ones, they can have better fracture resistance under bending (Sovják et al., 2017). It was concluded that this observation can result from the fact that short fibers have higher flexural properties. This finding agrees with the results of the present study, in which the longer the fibers are, the lower energy absorption and peak force they show under three-point bending loading. In another research, less uniform distribution of long fibers was used to justify the better mechanical performance of concrete reinforced with shorter fibers under three-point bending (Yoo et al., 2014).

In Section 3.4.3, it was understood that with the use of less tough shell (material mismatch 3), better energy absorption could be achieved. This observation can be put down to the fact that the crack propagates more easily through the shell, causing the debonding of the fiber from the concrete and increasing the toughness of the whole structure. Fig. 17 can also explain the fracture responses of the models which showed outstanding results in each material set. In the case of material set 4, due to a much higher critical energy release rate of the polypropylene fiber, the fibers are almost intact and the crack propagates through the shell and the concrete, resulting in higher energy absorption capacity and peak force. For the case of model 1 with material set 3, it can be seen that the crack has been considerably deflected. This is because of the fact that the shell has a lower critical energy release rate, and crack deflects to propagate through the shell, for which requires less energy. Nevertheless, for model 2 with material set 2, as the critical energy release rate of the shell and concrete are the same, the shell cannot deflect the crack and it propagates in a straight line, resulting in the breakage of the two fibers.

As it can be concluded from Fig. 16, in the material set 2 where the critical energy release rate of the shell is considered almost equal to that of the concrete, results vary mostly according to the l/d ratio rather than shell thickness, as the shell material is almost as tough as of the concrete. However, in the case of material set 3, both factors play an important role. MFRCs with the tough fiber (the material set 4), similar to the results under tensile and compressive loading, show a much higher capacity to undergo forces under three-point bending loading condition compared to other sets.

The higher flexural strength of MFRCs with polypropylene fibers is confirmed by a study into the effect of fiber length, where it is explained

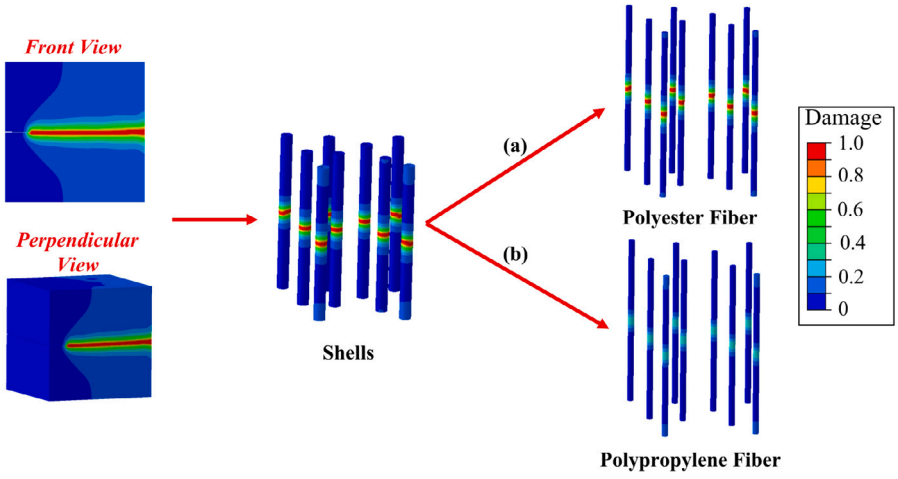

Fig. 21. The crack propagation through 3D MFRC models with (a) polyester fiber, (b) polypropylene fiber. Similar to 2D simulations, there is no fiber breakage in the case of polypropylene fibers, which results in a higher absorbed energy and peak force.

that an increase in the fiber length, can improve its flexural strength and fracture response (Bisaria et al., 2015). There have also been similar observations to the results discussed above in the experiments done by Han et al. (2019) and Aydın and Baradan (2013). However, in another study done on polyester fiber reinforced concrete by Sovják et al. (2017), the most favorable performance was reported by an approximate length of 14-mm fiber, which strengthens our findings for material sets 1–3, where the most favorable models had a fiber length of 12 mm. It was also explained by Yoo et al. (2015b, 2014), who studied the effect of the length of the polyester fibers in reinforced concrete, that longer fibers might result in a drop in the toughness of the entire structure. Our assumption is that, in the case of tough fibers (material set 4), as the fibers remain intact, the load-bearing mechanism is the crack deflection, which is provoked by the use of long fibers. In the case of polyester fiber (material sets 1–3), nonetheless, as the fiber breakage contributes to a great amount of absorbed energy, MFRCs with shorter fibers exhibit better fracture response. In agreement with the results shown by Sivakumar and Santhanam (2007a), polypropylene fiber reinforced concrete exhibit better fracture resistance and flexural strength than of polyester fiber reinforced concrete. In another study, it was suggested that polyester fibers can be most useful in terms of flexural strength when combined with steel fibers (Sivakumar and Santhanam, 2007b). The same conclusion was made in the work of Rostami et al. (2019), where it was proposed that polypropylene fiber reinforced concrete display the highest strength under three-point bending loads among non-metallic fibers.

4.4. 3D analysis of fracture response of MFRCs under tensile loading

Like it was discussed in Section 3.5, it was concluded when the majority of the fibers are placed perpendicularly to the pre-crack, MFRCs can absorb more energy. This can be attributed to the fact that the crack propagated through more shells and fibers, like it can be checked in Fig. 19. However, in the case of anti-parallel fibers, some shells and fibers remained intact as the crack did not propagate through them. In other words, since fiber direction is the same as the direction of the loading and the placement of the fibers is perpendicular to the pre-crack, through the toughening mechanism, not only is the elastic response intensified, but also there is more energy absorbed in the post-yielding region, as more fibers are engaged in the crack propagation path. Therefore, the amount of energy absorption through the model with perpendicular fibers is also more than the case of anti-parallel ones.

It was also confirmed again through the 3D analysis that by the use of polypropylene fibers, better fracture response is displayed by MFRCs. Fig. 21 can explain the underlying reason for the improvement. As the crack propagates through the concrete, it breaks the shell as well. However, in the case of polypropylene fiber, it does not break the polypropylene fibers, which results in a higher capacity for the energy absorption and the peak force that the structure can undergo due to having a more favorable elastic response and toughening mechanism. This is contrary to the case of polyester fiber, where the crack also propagates through the fibers. However, it must be mentioned that in the case of polypropylene fiber, the structure reaches failure at a slightly lower displacement load. We assume this might stem from the fact that polypropylene fibers are stiffer and can undergo less displacement. Additionally, in the case of polyester fibers, as fibers undergo breakage, strain hardening occurs and crack propagates a bit more slowly through the entire concrete block.

4.5. Limitations

It is also worth mentioning that our simulations come with some limitations. In the first and second case studies, 2D models of MFRCs were considered. In these case studies, crack propagation could happen along the longitudinal axis, which were not accounted for. Furthermore, like mentioned above, in our models, we presume that the interface of shell and concrete is perfect bonding, which is not able to capture the interface debonding. As a part of the future study, cohesive interface failure mechanisms can be incorporated in the phase-field fracture framework in order to look into the interface properties of shell-fiber and shell-concrete. Another limitation that we are faced with was regarding the length scale parameter (l_c). Even though it is still under debate (Zhang et al., 2017), this parameter, which is indicative of damage thickness, is also considered a material property and that it might require experimental work to be accurately determined (Pham et al., 2011; Sicsic and Marigo, 2013). However, in other studies, this parameter was regarded as a numerical parameter, and was selected to be smaller than the smallest characteristic length in the model (Nguyen and Niiranen, 2020; Kumar et al., 2022; Wu and Nguyen, 2018). In our study, it was also chosen based on the smallest length scale of the geometry and considerations for mesh size. Nevertheless, we want to remind that the purpose of this study was a parametric study to determine the most favorable configuration based on the geometrical characteristics of fibers and material mismatch effects. As it can be seen in Appendix B, changing the length scale parameter mainly scales up/down the force-displacement results. Hence, the findings of this study is not affected by the l_c parameter. Moreover, regarding the shell material, which is nitrocellulose in our ongoing experiments, there is no information available for its critical energy release rate. Therefore, there is uncertainty regarding its exact value, for which we tried to study the mismatch effects. In our future studies and experiments, we will further look into such uncertainty parameters and their effects on the fracture response of MFRCs.

5. Conclusion

A numerical study was conducted on MFRCs to predict their fracture properties under tensile, compressive, and flexural loading. The changing parameters between the models were the shell thickness, the ratio of fiber length to its diameter, and the material mismatch effects. Using observations made in this study, the following conclusions have been drawn:

- Under tensile loading condition, when polyester fiber is utilized in MFRCs, lower fiber length-to-diameter ratio and shell thickness showed the best performance. However, in the case of polypropylene fiber, higher length-to-diameter ratio and shell thickness showed the most favorable fracture response.
- Under compressive loading, for all material sets, MFRCs with the lowest fiber length-to-diameter ratio and shell thickness showed the highest peak force as well as absorbed energy, making the conclusion straightforward that the lower the ratio of fiber length to diameter and shell thickness, the better performance can be seen under compression.
- Under three-point bending, similar to tensile loading, it can be concluded that with polyester fiber, the lowest fiber length-to-diameter ratio shows the best fracture response.
- Less tough shell material showed the highest amount of absorbed energy for each model under three-point bending loading condition. This resulted from the debonding of the fibers from the concrete as crack propagated through the shells.
- In 3D phase-field modeling, it was seen that the more perpendicular the majority of fibers are placed to pre-crack, the higher peak force and energy absorption can be seen from the MFRCs under tensile loading.
- In the 3D models, similar to 2D analyses, polypropylene fibers remain intact as the crack propagates, which results in a better energy absorption as well as higher peak force.

Declaration of competing interest

The authors declare that they have no known competing financial interests or personal relationships that could have appeared to influence the work reported in this paper.

Data availability

Data will be made available on request.

Acknowledgments

The authors acknowledge the high-performance computing resources (PROTEUS: the Drexel Cluster) and support at the Drexel University. This work is supported by the National Science Foundation NSF, USA Award CMMI-2029555. This study was performed at Drexel University in the Multiscale Computational Mechanics and Biomechanics (MCMB) Lab. Any opinions, findings, and conclusions or recommendations expressed in this material are those of the authors and do not necessarily reflect the views of the National Science Foundation.

Appendix A. Expanding further on phase-field fracture framework

To couple the phase-field damage and displacement problems, the total potential energy in a cracked body takes the form

$$\Pi^{int} = E(\boldsymbol{u}, d) + W^{dmg}(d), \tag{A.1}$$

where $E(\boldsymbol{u}, d)$ is the elastic energy restored in the cracked body and $W^{dmg}(d)$ is the required energy to create cracks in the body. The elastic energy in the cracked body can be given by

$$E(\boldsymbol{u}, d) = \int_{\Omega} \Psi(\boldsymbol{\varepsilon}(\boldsymbol{u}), d)\, d\Omega, \tag{A.2}$$

where $\Psi(\boldsymbol{\varepsilon}(\boldsymbol{u}), d)$ is the strain energy density for the damaged body (Miehe et al., 2010), and it can be introduced by an anisotropic energy storage function such that

$$\Psi(\boldsymbol{\varepsilon}(\boldsymbol{u}), d) = g(d)\ \ \Psi_0^+(\boldsymbol{\varepsilon}) + \ \Psi_0^-(\boldsymbol{\varepsilon}), \tag{A.3}$$

This is based on an assumption which decomposes the stored energy Ψ_0 of the unbroken body into a positive mode $\Psi_0^+(\boldsymbol{\varepsilon})$ due to tension and a negative mode $\Psi_0^-(\boldsymbol{\varepsilon})$ due to compression as below

$$\Psi_0(\boldsymbol{\varepsilon}) = \ \Psi_0^+(\boldsymbol{\varepsilon}) + \ \Psi_0^-(\boldsymbol{\varepsilon}), \tag{A.4}$$

In Eq. (A.3), $\boldsymbol{\varepsilon}(\boldsymbol{u}) = (\nabla \boldsymbol{u} + \nabla \boldsymbol{u}^T)/2$ is the symmetric strain tensor and $g(d) = (1-d)^2 + k$ is known as the stress degradation function (Miehe et al., 2010). k is a small positive parameter to avoid the full degradation of the energy by marginal remaining of $k\Psi_0^+(\boldsymbol{\varepsilon})$ where the material is fully broken ($d = 1$). This parameter is chosen to be very small ($k \approx 0$) to maintain algebraically the implemented numerical equations well-conditioned for partially-broken systems (Miehe et al., 2010; Nguyen et al., 2016b). Note that the stress degradation function $g(d)$ only affects the positive part of the stored energy in the broken body. This simulates a realistic framework of fracture in which the crack cannot propagate where the strains are fully compressive. In the Eq. (A.4), $\Psi_0(\boldsymbol{\varepsilon}(\boldsymbol{u}))$ is the linear elastic strain energy density in the unbroken body

$$\Psi_0(\boldsymbol{\varepsilon}(\boldsymbol{u})) = \frac{1}{2}\boldsymbol{\varepsilon}^T \mathbf{C} \boldsymbol{\varepsilon}, \tag{A.5}$$

where $\mathbf{C}$ is the linear elastic stiffness matrix.

In the present work, the staggered solution is implemented (suggested by Molnár and Gravouil (2017)), where the two-field problem is decoupled to have a stable implicit formulation. This is due to the fact that it was shown in the problems with the unstable crack growth, the static monolithic solution becomes numerically unstable (Miehe et al., 2010). The coupled two-field problem can be separated into two independent minimization formulations, one formulation for the phase-field part and another for the displacement. Fig. 2 displays schematically the separated schemes, where the displacement field and the phase field can be linked together using a history field.

In the first problem, to solve the fracture topology, the energy functional related to the phase-field takes the form

$$\Pi^d = \int_{\Omega} \left(g_c \gamma(d, \nabla d) + (1-d^2)\, \mathcal{H} \right) d\Omega, \tag{A.6}$$

where $\mathcal{H}$ is defined as the strain history functional in order to satisfy the irreversibility of the damage evolution. Therefore, the history functional should meet the Kuhn–Tucker conditions (Molnár and Gravouil, 2017)

$$\Psi_0 - \mathcal{H} \le 0, \quad \dot{\mathcal{H}} \ge 0, \quad \dot{\mathcal{H}}(\Psi_0 - \mathcal{H}) = 0, \tag{A.7}$$

$\mathcal{H}$ introduces the maximum of the positive part of the strain energy density during loading applied within the time t_{n+1}

$$\mathcal{H}_{n+1} = \begin{cases} \Psi_0^+(\boldsymbol{\varepsilon}(\boldsymbol{u})) & if \ \ \Psi_0^+(\boldsymbol{\varepsilon}(\boldsymbol{u})) > \mathcal{H}_n \\ \mathcal{H}_n & if \ \ \Psi_0^+(\boldsymbol{\varepsilon}(\boldsymbol{u})) \le \mathcal{H}_n, \end{cases} \tag{A.8}$$

where $\mathcal{H}_n$ is the energy history field for the time t_n (previous increment).

In the second problem, by considering a fixed d, the energy functional for the displacement field is defined

$$\Pi^u \simeq E(\boldsymbol{u}, d) - W^{ext}, \tag{A.9}$$

where W^{ext} is the external work due to body forces and boundary tractions

$$W^{ext} = \int_{\Omega} \bar{\boldsymbol{b}}.\boldsymbol{u}\ d\Omega + \int_{\partial\Omega} \bar{\boldsymbol{t}}.\boldsymbol{u}\ d\partial\Omega, \tag{A.10}$$

where $\bar{\boldsymbol{b}}$ and $\bar{\boldsymbol{t}}$ are body forces and the boundary tractions, respectively. By substituting Eqs. (A.2) and (A.10) into Eq. (A.9), the following term can be obtained

$$\Pi^u = \int_{\Omega} (\Psi(\boldsymbol{\varepsilon}(\boldsymbol{u}), d) - \bar{\boldsymbol{b}}.\boldsymbol{u})\, d\Omega - \int_{\partial\Omega} \bar{\boldsymbol{t}}.\boldsymbol{u}\ d\partial\Omega. \tag{A.11}$$

Another point that is deemed important to draw attention to, is the fact that the phase-field framework has an edge over traditional gradient-based fracture methods, where it has been seen that spurious damage grows in the FEM (de Borst and Verhoosel, 2016; Poh and Sun, 2017; Loew et al., 2020; Duda et al., 2015). This is due to the fact that, the second term in the relation below, which is the thermodynamic driving force in phase-field fracture frameworks, vanishes as $d \to 0$:

$$d - f(d, G_c) = l^2 \nabla^2 d \tag{A.12}$$

Because this driving force rate approaches zero in highly damaged regions, the corresponding damage rate vanishes therewith, hence preventing further spreading of the damage process zone (Poh and Sun, 2017).

Appendix B. Analysis of mesh convergence and length scale parameter

In terms of finite element discretization, a certain minimum element size h must be considered (Miehe et al., 2010), which must satisfy

$$h < \frac{l_c}{2} \tag{B.1}$$

It is highly worthy of noting that this length scale parameter is believed to be a material property, which itself depends on other material parameters, such as elastic modulus, critical energy release rate, and yield stress (Mandal et al., 2019). The phase-field approach that has been implemented in the current study is sensitive to length scale parameter. Therefore, experiments can be conducted as a reference in order to determine the appropriate l_c for reinforced concrete. Nevertheless, in terms of the computational efficiency, it is worthy of mentioning that

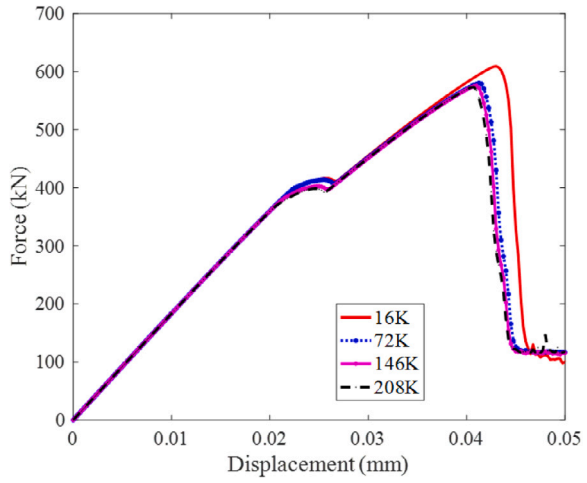

Fig. B.1. Mesh convergence for the model 1 using l_c = 0.01 mm. The same results have been observed for 72K, 146K, and 208K elements.

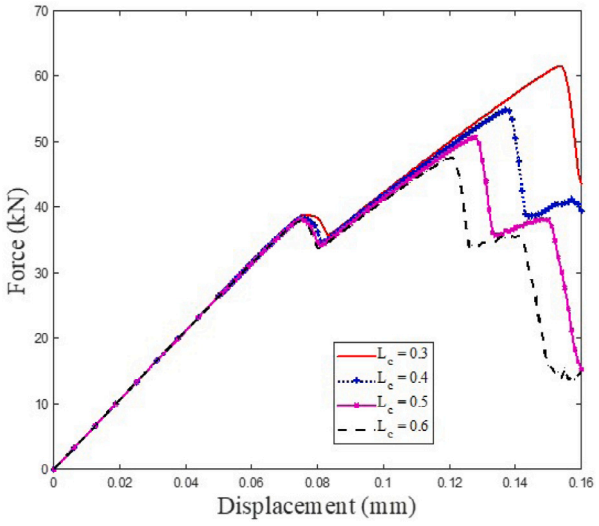

Fig. B.2. The impact of changes in parameter l_c on the force–displacement results. This parameter merely scales up/down the force–displacement for all models, and hence, it cannot influence the comparisons and major findings of the paper.

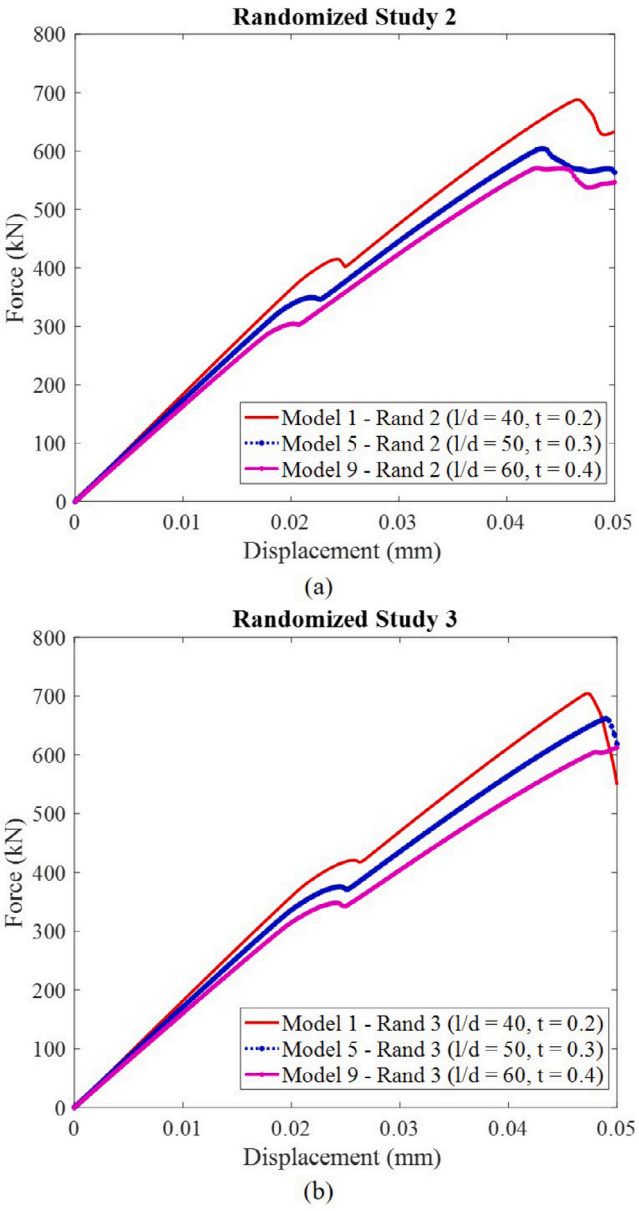

Fig. C.1. Force–displacement results of the second and third randomized study on the MFRCs under tension (a) Randomized study 2 (b) Randomized study 3. In all randomization studies, model 1 shows the most favorable results.

a small l_c can end up in an extremely fine mesh, causing a very high computational cost. One the other hand, it cannot be chosen to be very large, as it results in a large damage bandwidth, which cannot properly capture the crack propagation in shells and fibers. Consequently, it must be determined wisely based on the smallest scale in the geometry and considering the trade-off between the selected l_c and numerical simulations and their computational costs. As a result, for the simulations in the current paper, l_c has been considered based on the thickness of the shell and fibers as well as a reasonable computational cost.

Moreover, to ensure a converged solution, for the fracture of model 1 under tensile displacement loading with l_c = 0.01 mm shown in Fig. 5, we build four mesh networks containing approximately 16k, 72k, 146k, and 208k four-node elements (Fig. B.1). A better converged solution can be achieved by using quadratic elements (Tadepalli et al., 2011). In the cases with 72k, 146k, and 208k elements, the criterion (B.1) is satisfied only for the middle domain of the model, where the crack is expected to grow. Additionally, the criterion mentioned above is not satisfied in all regions of the models with 16k elements. The force–displacement results for the cases with 72k, 146k, and 208k are the same as it can be seen in Fig. B.1, as the criterion (B.1) is well satisfied for the region where crack propagates. Nevertheless, due to the departure from the criterion (B.1), there is a difference in the force–displacement result of the case with 16k elements. Thus, this mesh convergence study shows that the fracture solution for model 1 is converged in the cases with 72k, 146k, and 208k elements. Moreover, for each model in this study, mesh network is generated in a way that satisfies the minimum element size criterion (B.1) to ascertain the convergence of the solutions.

Furthermore, in order to see the impact of l_c parameter on the force–displacement results of the MFRCs, Fig. B.2 has been exhibited as below. As it was explained in the discussion, changes in this parameter mainly scales up/down the force–displacement results and do not impact the major findings and conclusions of the study.

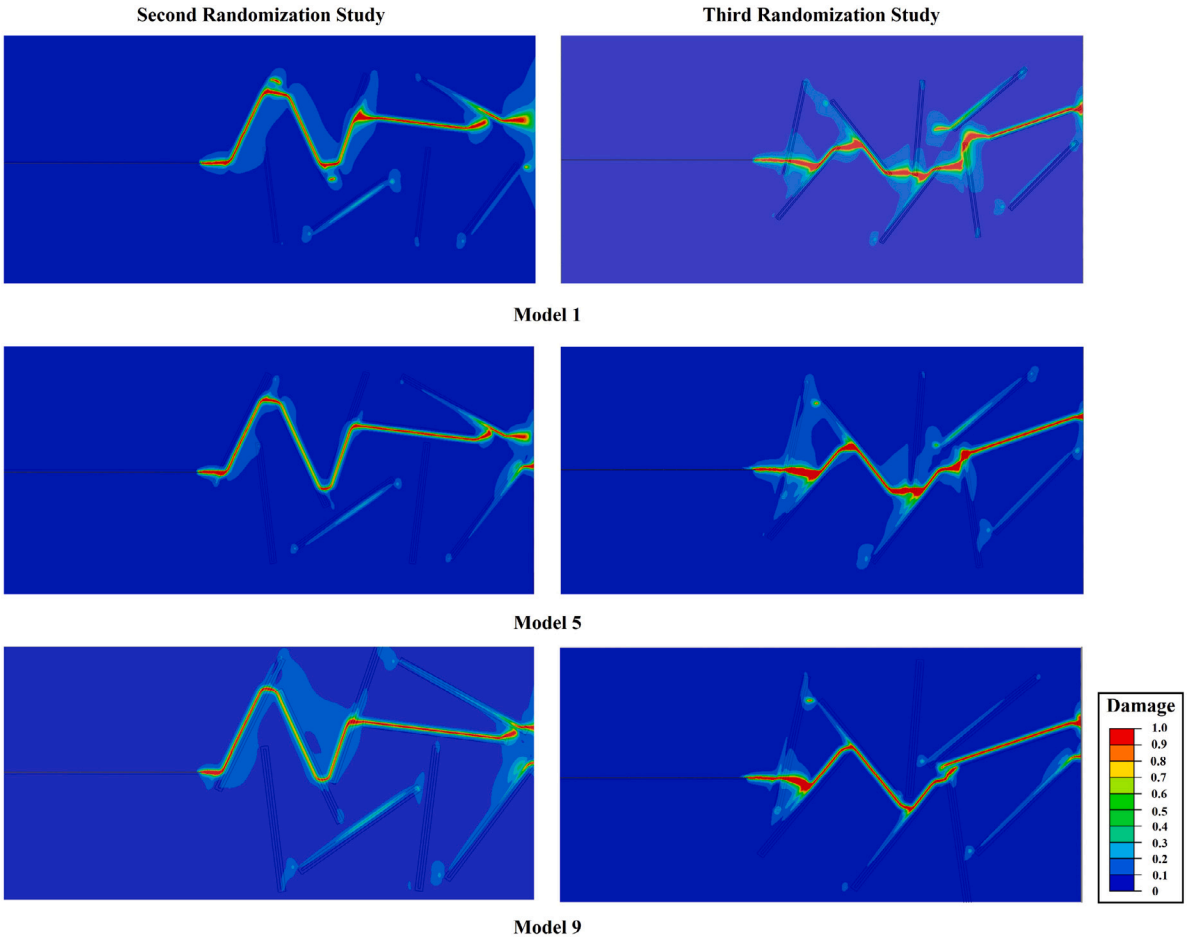

Fig. C.2. Crack propagation in the MFRCs under tension for the second and third randomized study.

Table C.1
The results of the randomized studies on the MFRCs under tension.

	Randomization 2		Randomization 3	
	Energy absorption (J)	Peak force (kN)	Energy absorption (J)	Peak force (kN)
Model 1	23.54	687.60	21.50	704.88
Model 5	20.59	603.89	19.77	661.84
Model 9	20.74	570.63	19.54	612.91

Appendix C. Randomization study

As it was mentioned in 3.1, in order to make sure that the conclusions made in this study are independent from the random distribution of the fibers and shells, two other randomized studies have been performed on Models 1, 5, and 9 in order to see if the results vary from the first randomized study. It is worth mentioning that the reason for choosing these three models is to take all levels of the factors into consideration (l/d = 40, 50, 60 and t = 0.2, 0.3, 0.4). The force–displacement results of the other two randomized studies can be checked in Fig. C.1, following Table C.1 which tabulates the peak force and energy absorption for these models. As it can be checked, model 1 still shows a higher peak force as well as energy absorption than the other two models, confirming the superiority of model 1 in the first randomized study. Therefore, it can be concluded that the results obtained are more dependent on the geometrical parameters and material properties of the fiber, shell, and concrete rather than the random distribution of the fibers and shells. The crack propagation through these models has been depicted for both randomized studies in Fig. C.2.

References

Abaqus, D., 2021. Abaqus 2021. Dassault Systemes Simulia Corporation, Providence, RI, USA, https://www.3ds.com/support/documentation/users-guides.

Al-Tabbaa, A., Litina, C., Giannaros, P., Kanellopoulos, A., Souza, L., 2019. First UK field application and performance of microcapsule-based self-healing concrete. Constr. Build. Mater. 208, 669–685.

Alam, S.Y., Loukili, A., 2020. Effect of micro-macro crack interaction on softening behaviour of concrete fracture. Int. J. Solids Struct. 182, 34–45.

Aldakheel, F., Hudobivnik, B., Hussein, A., Wriggers, P., 2018. Phase-field modeling of brittle fracture using an efficient virtual element scheme. Comput. Methods Appl. Mech. Engrg. 341, 443–466.

Ambati, M., Gerasimov, T., De Lorenzis, L., 2015. Phase-field modeling of ductile fracture. Comput. Mech. 55 (5), 1017–1040.

Areias, P.M., Belytschko, T., 2005. Analysis of three-dimensional crack initiation and propagation using the extended finite element method. Internat. J. Numer. Methods Engrg. 63 (5), 760–788.

Asferg, J.L., Poulsen, P.N., Nielsen, L.O., 2007. A direct XFEM formulation for modeling of cohesive crack growth in concrete. Comput. Concr. Int. J. 4 (2), 83–100.

ASTM-D5528, 2007. D5528-01,"Standard Test Method for Mode I Interlaminar Fracture Toughness of Unidirectional Fiber-Reinforced Polymer Matrix Composites". ASTM International, West Conshohocken, PA, http://dx.doi.org/10.1520/D5528-94A.

Aveston, J., Kelly, A., 1973. Theory of multiple fracture of fibrous composites. J. Mater. Sci. 8 (3), 352–362.

Aydın, S., Baradan, B., 2013. The effect of fiber properties on high performance alkali-activated slag/silica fume mortars. Composites B 45 (1), 63–69.

Babuška, I., Banerjee, U., 2012. Stable generalized finite element method (SGFEM). Comput. Methods Appl. Mech. Engrg. 201, 91–111.

Babuška, I., Banerjee, U., Osborn, J.E., 2003. Survey of meshless and generalized finite element methods: a unified approach. Acta Numer. 12, 1–125.

Banthia, N., 1994. Carbon fiber reinforced cements: structure, performance, applications and research needs. Spec. Publ. 142, 91–120.

Banthia, N., Moncef, A., Sheng, J., 1994. Uniaxial tensile response of cement composites reinforced with high volume fractions of carbon, steel, and polypropylene micro-fibers. Spec. Publ. 146, 43–68.

Banthia, N., Sheng, J., 1996. Fracture toughness of micro-fiber reinforced cement composites. Cem. Concr. Compos. 18 (4), 251–269.
Bărbuţă, M., Harja, M., Baran, I., 2010. Comparison of mechanical properties for polymer concrete with different types of filler. J. Mater. Civ. Eng. 22 (7), 696–701.
Bažant, Z.P., Oh, B.H., 1983. Crack band theory for fracture of concrete. Matér. Constr. 16 (3), 155–177.
Bažant, Z.P., Planas, J., 2019. Fracture and Size Effect in Concrete and Other Quasibrittle Materials. Routledge.
Beaumont, P., Soutis, C., Hodzic, A., 2015. Structural Integrity and Durability of Advanced Composites: Innovative Modelling Methods and Intelligent Design. Woodhead Publishing.
Bei-Xing, L., Ming-xiang, C., Fang, C., Lu-ping, L., 2004. The mechanical properties of polypropylene fiber reinforced concrete. J. Wuhan Univ. Technol. Mater. Sci. Ed. 19 (3), 68–71.
Belytschko, T., Gracie, R., 2007. On XFEM applications to dislocations and interfaces. Int. J. Plast. 23 (10–11), 1721–1738.
Bencardino, F., Rizzuti, L., Spadea, G., Swamy, R., 2010. Experimental evaluation of fiber reinforced concrete fracture properties. Composites B 41 (1), 17–24.
Bisaria, H., Gupta, M., Shandilya, P.a., Srivastava, R., 2015. Effect of fibre length on mechanical properties of randomly oriented short jute fibre reinforced epoxy composite. Mater. Today: Proc. 2 (4–5), 1193–1199.
Bolat, H., Şimşek, O., Çullu, M., Durmuş, G., Can, Ö., 2014. The effects of macro synthetic fiber reinforcement use on physical and mechanical properties of concrete. Composites B 61, 191–198.
Bourdin, B., Francfort, G.A., Marigo, J.-J., 2008. The variational approach to fracture. J. Elasticity 91 (1), 5–148.
Bui, T.Q., Hu, X., 2021. A review of phase-field models, fundamentals and their applications to composite laminates. Eng. Fract. Mech. 248, 107705.
Cao, Q., Sun, W., Guo, L., Zhang, G., 2012. Polymer-modified concrete with improved flexural toughness and mechanism analysis. J. Wuhan Univ. Technol. Mater. Sci. Ed. 27 (3), 597–601.
Cao, M., Xie, C., Guan, J., 2019. Fracture behavior of cement mortar reinforced by hybrid composite fiber consisting of CaCO3 whiskers and PVA-steel hybrid fibers. Composites A 120, 172–187.
Cervera, M., Barbat, G., Chiumenti, M., Wu, J.-Y., 2022. A comparative review of XFEM, mixed FEM and phase-field models for quasi-brittle cracking. Arch. Comput. Methods Eng. 29 (2), 1009–1083.
Chella Gifta, C., Prabavathy, S., 2018. Study on energy absorption capacity of steel–polyester hybrid fiber reinforced concrete under uni-axial compression. J. Inst. Eng. (India): Ser. A 99 (3), 547–553.
Chen, P.-W., Chung, D., 1996a. Comparative study of concretes reinforced with carbon, polyethylene, and steel fibers and their improvement by latex addition. Mater. J. 93 (2), 129–146.
Chen, P.-W., Chung, D., 1996b. Concrete as a new strain/stress sensor. Composites B 27 (1), 11–23.
Chen, P.-W., Fu, X., Chung, D., 1997. Microstructural and mechanical effects of latex, methylcellulose, and silica fume on carbon fiber reinforced cement. Mater. J. 94 (2), 147–155.
Colombo, D., 2012. An implicit geometrical approach to level sets update for 3D non planar X-FEM crack propagation. Comput. Methods Appl. Mech. Engrg. 237, 39–50.
De Belie, N., Gruyaert, E., Al-Tabbaa, A., Antonaci, P., Baera, C., Bajare, D., Darquennes, A., Davies, R., Ferrara, L., Jefferson, T., et al., 2018. A review of self-healing concrete for damage management of structures. Adv. Mater. Interfaces 5 (17), 1800074.
de Borst, R., Verhoosel, C.V., 2016. Gradient damage vs phase-field approaches for fracture: Similarities and differences. Comput. Methods Appl. Mech. Engrg. 312, 78–94.
Deng, Z., 2005. The fracture and fatigue performance in flexure of carbon fiber reinforced concrete. Cem. Concr. Compos. 27 (1), 131–140.
Duarte, C.A., Hamzeh, O., Liszka, T., Tworzydlo, W., 2001. A generalized finite element method for the simulation of three-dimensional dynamic crack propagation. Comput. Methods Appl. Mech. Engrg. 190 (15–17), 2227–2262.
Duda, F.P., Ciarbonetti, A., Sánchez, P.J., Huespe, A.E., 2015. A phase-field/gradient damage model for brittle fracture in elastic–plastic solids. Int. J. Plast. 65, 269–296.
Elices, M., Guinea, G., Gomez, J., Planas, J., 2002. The cohesive zone model: advantages, limitations and challenges. Eng. Fract. Mech. 69 (2), 137–163.
Elices, M., Rocco, C., Roselló, C., 2009. Cohesive crack modelling of a simple concrete: Experimental and numerical results. Eng. Fract. Mech. 76 (10), 1398–1410.
Feng, D.-C., Wu, J.-Y., 2018. Phase-field regularized cohesive zone model (CZM) and size effect of concrete. Eng. Fract. Mech. 197, 66–79.
Ferrara, L., Krelani, V., Moretti, F., 2016. Autogenous healing on the recovery of mechanical performance of high performance fibre reinforced cementitious composites (HPFRCCs): Part 2–correlation between healing of mechanical performance and crack sealing. Cem. Concr. Compos. 73, 299–315.
Fu, X., Chung, D., 1996. Self-monitoring of fatigue damage in carbon fiber reinforced cement. Cem. Concr. Res. 26 (1), 15–20.
Giannaros, P., Kanellopoulos, A., Al-Tabbaa, A., 2016. Sealing of cracks in cement using microencapsulated sodium silicate. Smart Mater. Struct. 25 (8), 084005.
Gilabert, F., Garoz, D., Van Paepegem, W., 2017. Numerical study of transitional brittle-to-ductile debonding of a capsule embedded in a matrix. Compos. Interfaces 24 (1), 69–84.
Gordeliy, E., Abbas, S., Peirce, A., 2019. Modeling nonplanar hydraulic fracture propagation using the XFEM: An implicit level-set algorithm and fracture tip asymptotics. Int. J. Solids Struct. 159, 135–155.
Gordeliy, E., Peirce, A., 2013. Coupling schemes for modeling hydraulic fracture propagation using the XFEM. Comput. Methods Appl. Mech. Engrg. 253, 305–322.
Gordeliy, E., Peirce, A., 2015. Enrichment strategies and convergence properties of the XFEM for hydraulic fracture problems. Comput. Methods Appl. Mech. Engrg. 283, 474–502.
Graham, R.K., Huang, B., Shu, X., Burdette, E.G., 2013. Laboratory evaluation of tensile strength and energy absorbing properties of cement mortar reinforced with micro-and meso-sized carbon fibers. Constr. Build. Mater. 44, 751–756.
Grzybowski, M., Shah, S.P., 1990. Shrinkage cracking of fiber reinforced concrete. Mater. J. 87 (2), 138–148.
Gupta, S., Dai Pang, S., Kua, H.W., 2017. Autonomous healing in concrete by bio-based healing agents–A review. Constr. Build. Mater. 146, 419–428.
Han, J., Zhao, M., Chen, J., Lan, X., 2019. Effects of steel fiber length and coarse aggregate maximum size on mechanical properties of steel fiber reinforced concrete. Constr. Build. Mater. 209, 577–591.
Hashemi, S., Kinloch, A., Williams, J., 1989. Corrections needed in double-cantilever beam tests for assessing the interlaminar failure of fibre-composites. J. Mater. Sci. Lett. 8, 125–129.
Jirásek, M., Belytschko, T., 2002. Computational resolution of strong discontinuities. In: Proceedings of Fifth World Congress on Computational Mechanics, WCCM V, Vienna University of Technology, Austria. Citeseer.
Jirásek, M., Zimmermann, T., 1998. Analysis of rotating crack model. J. Eng. Mech. 124 (8), 842–851.
Josephson, T.O., Moore, J.P., Maghami, E., Freeman, T.A., Najafi, A.R., 2022. Computational study of the mechanical influence of lacunae and perilacunar zones in cortical bone microcracking. J. Mech. Behav. Biomed. Mater. 126, 105029.
Karihaloo, B.L., Xiao, Q., 2003. Modelling of stationary and growing cracks in FE framework without remeshing: a state-of-the-art review. Comput. Struct. 81 (3), 119–129.
Khan, M., Cao, M., Xie, C., Ali, M., 2021. Efficiency of basalt fiber length and content on mechanical and microstructural properties of hybrid fiber concrete. Fatigue Fract. Eng. Mater. Struct. 44 (8), 2135–2152.
Khisamitov, I., Meschke, G., 2018. Variational approach to interface element modeling of brittle fracture propagation. Comput. Methods Appl. Mech. Engrg. 328, 452–476.
Kizilkanat, A.B., 2016. Experimental evaluation of mechanical properties and fracture behavior of carbon fiber reinforced high strength concrete. Period. Polytech. Civ. Eng. 60 (2), 289–296.
Kizilkanat, A.B., Kabay, N., Akyüncü, V., Chowdhury, S., Akça, A.H., 2015. Mechanical properties and fracture behavior of basalt and glass fiber reinforced concrete: An experimental study. Constr. Build. Mater. 100, 218–224.
Koniki, S., Prasad, D.R., 2019. Influence of hybrid fibres on strength and stress-strain behaviour of concrete under uni-axial stresses. Constr. Build. Mater. 207, 238–248.
Kozlowski, M., Kadela, M., Gwozdz-Lason, M., 2016. Numerical fracture analysis of foamed concrete beam using XFEM method. In: Applied Mechanics and Materials, Vol. 837. Trans Tech Publ, pp. 183–186.
Kumar, A., Ravi-Chandar, K., Lopez-Pamies, O., 2022. The revisited phase-field approach to brittle fracture: application to indentation and notch problems. Int. J. Fract. 237 (1–2), 83–100.
Lee, S.F., Jacobsen, S., 2011. Study of interfacial microstructure, fracture energy, compressive energy and debonding load of steel fiber-reinforced mortar. Mater. Struct. 44 (8), 1451–1465.
Li, V.C., Wang, S., Wu, C., 2001. Tensile strain-hardening behavior of polyvinyl alcohol engineered cementitious composite (PVA-ECC). Mater. J. 98 (6), 483–492.
Li, V.C., Wu, C., Wang, S., Ogawa, A., Saito, T., 2002. Interface tailoring for strain-hardening polyvinyl alcohol-engineered cementitious composite (PVA-ECC). Mater. J. 99 (5), 463–472.
Li, X., Xu, Y., 2022. Phase field modeling scheme with mesostructure for crack propagation in concrete composite. Int. J. Solids Struct. 234, 111259.
Loew, P.J., Peters, B., Beex, L.A., 2020. Fatigue phase-field damage modeling of rubber using viscous dissipation: Crack nucleation and propagation. Mech. Mater. 142, 103282.
Lyu, D., Fan, H., Li, S., 2016. A hierarchical multiscale cohesive zone model and simulation of dynamic fracture in metals. Eng. Fract. Mech. 163, 327–347.
Maghami, E., Josephson, T.O., Moore, J.P., Rezaee, T., Freeman, T.A., Karim, L., Najafi, A.R., 2021a. Fracture behavior of human cortical bone: Role of advanced glycation end-products and microstructural features. J. Biomech. 125, 110600.
Maghami, E., Moore, J.P., Josephson, T.O., Najafi, A.R., 2022. Damage analysis of human cortical bone under compressive and tensile loadings. Comput. Methods Biomech. Biomed. Eng. 25 (3), 342–357.
Maghami, E., Najafi, A.R., 2022. Influence of age-related changes on crack growth trajectories and toughening mechanisms in human dentin. Dent. Mater..
Maghami, E., Pejman, R., Najafi, A.R., 2021b. Fracture micromechanics of human dentin: A microscale numerical model. J. Mech. Behav. Biomed. Mater. 114, 104171.
Mandal, T.K., Nguyen, V.P., Wu, J.-Y., 2019. Length scale and mesh bias sensitivity of phase-field models for brittle and cohesive fracture. Eng. Fract. Mech. 217, 106532.
Mansour, R., El Abidine, R.Z., Brahim, B., 2017. Performance of polymer concrete incorporating waste marble and alfa fibers. Adv. Concr. Constr. 5 (4), 331.

MATLAB, 2021. Version 9.12.0 (R2022a). The MathWorks Inc., Natick, Massachusetts.
Matvienko, Y.G., 1999. On the cohesive zone model for a finite crack. Int. J. Fract. 98 (3), 53–58.
Meng, X., Bai, E., Wang, Z., Huang, Z., Xia, W., 2021. Study on splitting tensile mechanical properties of carbon fiber/polymer latex powder composite modified concrete. In: E3S Web of Conferences, Vol. 261. EDP Sciences, p. 02036.
Miehe, C., Hofacker, M., Welschinger, F., 2010. A phase field model for rate-independent crack propagation: Robust algorithmic implementation based on operator splits. Comput. Methods Appl. Mech. Engrg. 199 (45–48), 2765–2778.
Mignon, A., Graulus, G.-J., Snoeck, D., Martins, J., De Belie, N., Dubruel, P., Van Vlierberghe, S., 2015. pH-sensitive superabsorbent polymers: a potential candidate material for self-healing concrete. J. Mater. Sci. 50 (2), 970–979.
Milla, J., Hassan, M.M., Rupnow, T., Daly, W.H., 2019. Measuring the crack-repair efficiency of steel fiber reinforced concrete beams with microencapsulated calcium nitrate. Constr. Build. Mater. 201, 526–538.
Mindess, S., 2008. Fibrous concrete reinforcement. In: Developments in the Formulation and Reinforcement of Concrete. Woodhead Publishing Limited, Cambridge, England, pp. 154–166.
Mobasher, B., Li, C.Y., 1996. Mechanical properties of hybrid cement-based composites. ACI Mater. J. 93, 284–292.
Molnár, G., Gravouil, A., 2017. 2D and 3D abaqus implementation of a robust staggered phase-field solution for modeling brittle fracture. Finite Elem. Anal. Des. 130, 27–38.
Natarajan, S., Annabattula, R.K., Martínez-Pañeda, E., et al., 2019. Phase field modelling of crack propagation in functionally graded materials. Composites B 169, 239–248.
Nguyen, T.H., Niiranen, J., 2020. A second strain gradient damage model with a numerical implementation for quasi-brittle materials with micro-architectures. Math. Mech. Solids 25 (3), 515–546.
Nguyen, T.-T., Waldmann, D., Bui, T.Q., 2020. Phase field simulation of early-age fracture in cement-based materials. Int. J. Solids Struct. 191, 157–172.
Nguyen, T.T., Yvonnet, J., Bornert, M., Chateau, C., Sab, K., Romani, R., Le Roy, R., 2016a. On the choice of parameters in the phase field method for simulating crack initiation with experimental validation. Int. J. Fract. 197, 213–226.
Nguyen, T.-T., Yvonnet, J., Zhu, Q.-Z., Bornert, M., Chateau, C., 2016b. A phase-field method for computational modeling of interfacial damage interacting with crack propagation in realistic microstructures obtained by microtomography. Comput. Methods Appl. Mech. Engrg. 312, 567–595.
Owens, P., Newman, J., Choo, B., 2003. Advanced concrete technology processes.
Park, K., Paulino, G.H., 2011. Cohesive zone models: a critical review of traction-separation relationships across fracture surfaces. Appl. Mech. Rev. 64 (6).
Park, K., Paulino, G.H., Roesler, J., 2010. Cohesive fracture model for functionally graded fiber reinforced concrete. Cem. Concr. Res. 40 (6), 956–965.
Pham, K., Amor, H., Marigo, J.-J., Maurini, C., 2011. Gradient damage models and their use to approximate brittle fracture. Int. J. Damage Mech. 20 (4), 618–652.
Poh, L.H., Sun, G., 2017. Localizing gradient damage model with decreasing interactions. Internat. J. Numer. Methods Engrg. 110 (6), 503–522.
Prasad, M.S., Venkatesha, C., Jayaraju, T., et al., 2011. Experimental methods of determining fracture toughness of fiber reinforced polymer composites under various loading conditions. J. Miner. Mater. Charact. Eng. 10 (13), 1263.
Qian, C., Stroeven, P., 2000. Development of hybrid polypropylene-steel fibre-reinforced concrete. Cem. Concr. Res. 30 (1), 63–69.
Qureshi, T., Kanellopoulos, A., Al-Tabbaa, A., 2019. Autogenous self-healing of cement with expansive minerals-II: Impact of age and the role of optimised expansive minerals in healing performance. Constr. Build. Mater. 194, 266–275.
Rabczuk, T., Zi, G., Bordas, S., Nguyen-Xuan, H., 2008. A geometrically non-linear three-dimensional cohesive crack method for reinforced concrete structures. Eng. Fract. Mech. 75 (16), 4740–4758.
Ren, X., Li, J., 2013. Multi-scale based fracture and damage analysis of steel fiber reinforced concrete. Eng. Fail. Anal. 35, 253–261.
Rostami, R., Zarrebini, M., Mandegari, M., Sanginabadi, K., Mostofinejad, D., Abtahi, S.M., 2019. The effect of concrete alkalinity on behavior of reinforcing polyester and polypropylene fibers with similar properties. Cem. Concr. Compos. 97, 118–124.
Roth, S.-N., Léger, P., Soulaïmani, A., 2015. A combined XFEM–damage mechanics approach for concrete crack propagation. Comput. Methods Appl. Mech. Engrg. 283, 923–955.
Rots, J.G., Nauta, P., Kuster, G., Blaauwendraad, J., 1985. Smeared crack approach and fracture localization in concrete. HERON 30 (1), 1985.
Schlangen, E., 1995. Experimental and numerical analysis of fracture processes in concrete.
Schröder, J., Pise, M., Brands, D., Gebuhr, G., Anders, S., 2022. Phase-field modeling of fracture in high performance concrete during low-cycle fatigue: Numerical calibration and experimental validation. Comput. Methods Appl. Mech. Engrg. 398, 115181.
Shah, S.P., 1990. Determination of fracture parameters (K Ic s and CTODc) of plain concrete using three-point bend tests. Mater. Struct. 23 (6), 457–460.
Shah, A.A., Ribakov, Y., 2011. Recent trends in steel fibered high-strength concrete. Mater. Des. 32 (8–9), 4122–4151.
Shokrieh, M., Heidari-Rarani, M., Ayatollahi, M., 2012. Delamination R-curve as a material property of unidirectional glass/epoxy composites. Mater. Des. 34, 211–218.
Sicsic, P., Marigo, J.-J., 2013. From gradient damage laws to Griffith's theory of crack propagation. J. Elasticity 113, 55–74.
Sivakumar, A., Santhanam, M., 2007a. Mechanical properties of high strength concrete reinforced with metallic and non-metallic fibres. Cem. Concr. Compos. 29 (8), 603–608.
Sivakumar, A., Santhanam, M., 2007b. A quantitative study on the plastic shrinkage cracking in high strength hybrid fibre reinforced concrete. Cem. Concr. Compos. 29 (7), 575–581.
Snoeck, D., Van den Heede, P., Van Mullem, T., De Belie, N., 2018. Water penetration through cracks in self-healing cementitious materials with superabsorbent polymers studied by neutron radiography. Cem. Concr. Res. 113, 86–98.
Sovják, R., Máca, P., Imlauf, T., 2017. Effect of fibre length on the fracture energy of UHPFRC. Procedia Eng. 193, 74–79.
Stroeven, P., Babut, R., 1986. Fracture mechanics and structural aspects of concrete. Heron 31 (2), 15–44.
Strouboulis, T., Copps, K., Babuška, I., 2000. The generalized finite element method: an example of its implementation and illustration of its performance. Internat. J. Numer. Methods Engrg. 47 (8), 1401–1417.
Stynoski, P., Mondal, P., Marsh, C., 2015. Effects of silica additives on fracture properties of carbon nanotube and carbon fiber reinforced portland cement mortar. Cem. Concr. Compos. 55, 232–240.
Sukumar, N., Moës, N., Moran, B., Belytschko, T., 2000. Extended finite element method for three-dimensional crack modelling. Internat. J. Numer. Methods Engrg. 48 (11), 1549–1570.
Sun, Z., Xu, Q., 2008. Micromechanical analysis of polyacrylamide-modified concrete for improving strengths. Mater. Sci. Eng. A 490 (1–2), 181–192.
Swamy, R., 1979. Fracture mechanics applied to concrete. In: Dev. Concr. Technol.. Part I, 221–281.
Tadepalli, S.C., Erdemir, A., Cavanagh, P.R., 2011. Comparison of hexahedral and tetrahedral elements in finite element analysis of the foot and footwear. J. Biomech. 44 (12), 2337–2343.
Tanné, E., Li, T., Bourdin, B., Marigo, J.-J., Maurini, C., 2018. Crack nucleation in variational phase-field models of brittle fracture. J. Mech. Phys. Solids 110, 80–99.
Turgay, T., Polat, Z., Koksal, H., Doran, B., Karakoç, C., 2010. Compressive behavior of large-scale square reinforced concrete columns confined with carbon fiber reinforced polymer jackets. Mater. Des. 31 (1), 357–364.
Unger, J.F., Eckardt, S., Könke, C., 2007. Modelling of cohesive crack growth in concrete structures with the extended finite element method. Comput. Methods Appl. Mech. Engrg. 196 (41–44), 4087–4100.
Urata, S., Li, S., 2017. Higher order Cauchy–Born rule based multiscale cohesive zone model and prediction of fracture toughness of silicon thin films. Int. J. Fract. 203 (1), 159–181.
Wu, J.-Y., Chen, W.-X., 2022. On the phase-field modeling of fully coupled chemo-mechanical deterioration and fracture in calcium leached cementitious solids. Int. J. Solids Struct. 238, 111380.
Wu, J.-Y., Nguyen, V.P., 2018. A length scale insensitive phase-field damage model for brittle fracture. J. Mech. Phys. Solids 119, 20–42.
Xia, L., Da, D., Yvonnet, J., 2018. Topology optimization for maximizing the fracture resistance of quasi-brittle composites. Comput. Methods Appl. Mech. Engrg. 332, 234–254.
Xue, C., Li, W., Li, J., Tam, V.W., Ye, G., 2019. A review study on encapsulation-based self-healing for cementitious materials. Struct. Concr. 20 (1), 198–212.
Xue, C., Li, W., Wang, K., Sheng, D., Shah, S.P., 2020. Novel experimental and numerical investigations on bonding behaviour of crack interface in smart self-healing concrete. Smart Mater. Struct. 29 (8), 085004.
Yang, Z.-J., Li, B.-B., Wu, J.-Y., 2019. X-ray computed tomography images based phase-field modeling of mesoscopic failure in concrete. Eng. Fract. Mech. 208, 151–170.
Yoo, D.-Y., Kang, S.-T., Yoon, Y.-S., 2014. Effect of fiber length and placement method on flexural behavior, tension-softening curve, and fiber distribution characteristics of UHPFRC. Constr. Build. Mater. 64, 67–81.
Yoo, D.-Y., Lee, J.-H., Yoon, Y.-S., 2013. Effect of fiber content on mechanical and fracture properties of ultra high performance fiber reinforced cementitious composites. Compos. Struct. 106, 742–753.
Yoo, D.-Y., Yoon, Y.-S., Banthia, N., 2015a. Predicting the post-cracking behavior of normal-and high-strength steel-fiber-reinforced concrete beams. Constr. Build. Mater. 93, 477–485.
Yoo, D.-Y., Zi, G., Kang, S.-T., Yoon, Y.-S., 2015b. Biaxial flexural behavior of ultra-high-performance fiber-reinforced concrete with different fiber lengths and placement methods. Cem. Concr. Compos. 63, 51–66.
You, R., Li, D., Ngamkhanong, C., Janeliukstis, R., Kaewunruen, S., 2017. Fatigue life assessment method for prestressed concrete sleepers. Front. Built Environ. 3, 68.
Zhang, Z., Hsu, C.-T.T., 2005. Shear strengthening of reinforced concrete beams using carbon-fiber-reinforced polymer laminates. J. Compos. Constr. 9 (2), 158–169.
Zhang, W., Tang, Z., 2021. Numerical modeling of response of CFRP–concrete interfaces subjected to fatigue loading. J. Compos. Constr. 25 (5), 04021043.
Zhang, X., Vignes, C., Sloan, S.W., Sheng, D., 2017. Numerical evaluation of the phase-field model for brittle fracture with emphasis on the length scale. Comput. Mech. 59, 737–752.
Zhou, S., Rabczuk, T., Zhuang, X., 2018. Phase field modeling of quasi-static and dynamic crack propagation: COMSOL implementation and case studies. Adv. Eng. Softw. 122, 31–49.